CHAPTER 2

Micromanipulation in Mechanical Characterisation of Single Particles

Z. Zhang*, J.D. Stenson and **C.R. Thomas**

Contents

School of Chemical Engineering, University of Birmingham, Edgbaston, Birmingham B15 2TT, UK

*Corresponding author.
E-mail address: Z.Zhang@bham.ac.uk

Advances in Chemical Engineering, Volume 37
ISSN: 0065-2377, DOI 10.1016/S0065-2377(09)03702-8

Abstract

Many functional industrial products are in the form of microscopic particles. Mechanical characterisation of these particles is essential if physical damage to them in manufacturing processes is to be minimised, and their performance is to be optimised. Several experimental techniques can be used to characterise the mechanical properties of single microparticles, including micropipette aspiration, particle poking, atomic force microscopy, optical trapping and diametrical compression. The details of these techniques and their applications are presented in this review. Among them, diametrical compression has many advantages. It is capable of determining the mechanical properties of both biological and non-biological particles as small as 400 nm in diameter, and can be used for measurements at high deformations, including up to rupture. The technique can be enhanced by mathematical modelling to allow intrinsic mechanical properties to be estimated, for example, the particle (or particle wall) elastic modulus, and viscoelastic and plastic parameters. For biological materials, present and potential applications include studying mechanical damage to animal cells in suspension cultures, yeast and bacterial disruption in downstream processing equipment, changes of the morphology of filamentous microorganisms in submerged fermentations, plant cell behaviour in food processing, flocculation processes, cell mechanics, biomaterials and tissue engineering. For non-biological materials, applications include understanding and controlling particle breakage in processing equipment, handling and transport, and end-use applications.

1. INTRODUCTION

Both biological and non-biological microscopic particles (or microparticles) are used to produce functional products over a wide range of industrial sectors including chemical, agrochemical, food and feed, pharmaceutical and medical, human care and household care. These particles should have desirable structures and properties, for example, the appropriate size, porosity, mechanical strength and surface charge. Understanding the mechanical properties of microparticles is essential to predict their behaviour in manufacturing, and their performance in end-use applications.

In principle, the mechanical properties of particles can be determined by measuring their deformation under a mechanical load. This may be realised on single particles or a population. Mechanical characterisation of single particles is relatively difficult, particularly when their sizes are in the micro or nano ranges. The basis of many techniques for mechanical characterisation of single particles is micromanipulation. This can be used to perform a variety of mechanical operations on tiny objects under high magnification through the use of manipulators and a microscope (Madgar et al., 1996). Typical examples are the use of a micropipette to inject a single sperm into an ovum to aid fertilisation, and moving a single cell/particle in suspension from one location to another using optical trapping. Combination of micromanipulation of single particles with force measurement has enabled characterisation of the mechanical properties of micro/nanoparticles.

2. DESCRIPTION OF THE TECHNIQUES

The techniques that have been used to characterise the mechanical properties of microparticles may be classified as indirect and direct. The former includes measurement of breakage in a ''shear'' device, for example, a stirred vessel (Poncelet and Neufeld, 1989) or bubble column (Lu et al., 1992). However, the results from these indirect techniques are rather difficult to use since the mechanical breakage depends not only on the mechanical properties but also the hydrodynamics of the processing equipment, and the latter are still not well understood. To overcome this problem, a cone and plate viscometer that can apply well-defined shear stresses has been used to study breakage of hybridomas (Born et al., 1992), but this is not a widely applied or applicable technique because the forces are too small to break most cells.

Another possibility is to compress a layer of particles between two glass plates with a given applied force (Ohtsubo et al., 1991). The percentage of particle breakage can be related to the force. This gives some global measure of the strength of a sample of particles.

For biological particles, for example, cells which have a semi-permeable membrane and semi-permeable microcapsules, their mechanical integrity can be characterised by exposuring them to media with different osmotic pressures (Van Raamsdonk and Chang, 2001).

None of these indirect techniques relate the breakage of an individual particle to its mechanical properties. To achieve this, direct techniques are required. These are described later, and their capabilities and limitations discussed. Direct techniques also allow more sophisticated mathematical modelling to be undertaken, which is particularly valuable when the particles are not homogeneous, for example, cells with walls and membranes surrounding cytoplasm, or a liquid-filled microcapsule.

2.1 Pressure probe

The pressure probe is frequently used to study the hydraulic behaviour of plant tissues and individual cells, and their response to water stress.

High turgor (hydrostatic) pressures within cells lead to tensions in the cell wall, which maintain the cellular shape and function. Turgor pressure measurements can provide useful information about the physiology of cells.

In this technique, a capillary probe penetrates a cell, usually in a tissue, and allows the turgor pressure to be measured. It is assumed that the penetration of the cell does not affect the mechanical behaviour of the cell wall. By manipulating the pressure within the cell it is possible to derive the ''volumetric elastic modulus'' of the cell (Tomos, 2000; Tomos and Leigh, 1999). The primary use of the volumetric elastic modulus is to describe water transport in plant cells under non-steady conditions (Cosgrove, 1988). This parameter is often confused with the bulk elastic modulus, which (in solid mechanics) relates the fractional volumetric change of a solid to some external pressure change. However, in studies of plant–water relations, the mass of the cell is not conserved, and this definition of the bulk elastic modulus is invalid. Owing to this confusion, the volumetric elastic modulus has been described as physically ''meaningless'' (Wu et al., 1985), which is correct in relation to conventional mechanical analysis, notwithstanding the term still being of value in plant physiology.

Wang et al. (2006b) used the pressure probe to determine the internal turgor pressure and volumetric elastic modulus of single tomato cells from suspension cultures, rather than cells from tissues. However, this single cell technique is limited to cells over ca. 20 μm in diameter, because otherwise it would be challenging to obtain a sufficiently small probe, which would in any case probably block when it penetrates the cell wall. Besides, cell deformations achievable with a pressure probe are not great enough to cause cell failure.

2.2 Micropipette aspiration

The mechanical behaviour of living cells has been studied widely using the micropipette aspiration technique. In the most common application, a cell suspended in solution is partially or wholly aspirated into the mouth of a pipette (Figure 1). The inner diameter of the pipette may range from less than 1 μm to 10 μm (Lim et al., 2006). Video microscopy is used to record the change in shape of the cell as it is drawn into the micropipette, and the edges of the cell can be tracked to an accuracy of less than 25 nm. Measuring the elongation and suction pressure allows the mechanical properties of the cell to be determined, using a mechanical model of the behaviour (Hochmuth, 2000).

Micropipette aspiration has been used widely to measure the mechanical properties of many types of cells including red blood cells (RBCs), leukocytes and chondrocytes (Lim et al., 2006). One important

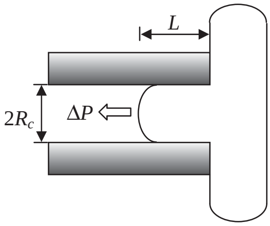

Figure 1 Diagram of the micropipette aspiration technique (modified from Lim et al., 2006). L is the length of extension into the pipette, R_c the inner radius of the pipette and ΔP the suction pressure.

application of the micropipette aspiration technique involves measuring the Poisson ratio of biological cells. Recently, He et al. (2007) used analytical simulations and finite element analysis to determine the Poisson ratio and elastic modulus of a single neutrophil cell wholly aspirated into a tapered cylindrical micropipette. Boudou et al. (2006) have also presented a finite element method for determining the Poisson ratio and Young's modulus of biological films; though this method was only implemented on polyacrylamide gels.

Compared to atomic force microscopy (AFM) or optical tweezers (described later) the micropipette aspiration technique appears simple. However, a major disadvantage of this method is the friction that occurs between the cell membrane and the glass pipette; accounting for this is difficult. In addition, the pipette aspiration technique produces stress concentrations at the edge of the pipette and the cell membrane. Recent advances in the use of finite element analyses have made it possible to allow for these stress concentrations, although direct measurement of the forces is impossible (Boudou et al., 2006). Other disadvantages of micropipette aspiration are that curvature in the cell membrane as it is drawn into the pipette can cause damage to the cell, that it has only been used on cells that are large and easily deformable, and that it does not allow failure criteria to be determined, which is essential for improving our understanding of cell disruption.

2.3 Cell poking and atomic force microscopy (AFM)

The cell poking technique involves the indentation of a cell with a micro tip of a probe and measuring the loading and unloading forces involved. Owing to the localised bending that this causes within the cell wall, analysis of this method would require the use of a very complicated mechanical model (Daily et al., 1984; Duszyk et al., 1989). Cell poking has been used to measure the mechanical response of a number of mammalian cell types including erythrocytes (Daily et al., 1984), and stretching and breaking events of plant cell walls leading to determination of mean cell diameter and cell wall fracture energy (Hiller et al., 1996). Goldman (2000) showed that cell poking, when used in conjunction with AFM, could be used to obtain qualitative information about the mechanical properties of mouse embryonic carcinoma cells. However, cell poking has largely been supplanted by the use of AFM using probes significantly smaller than the sample to determine local mechanical properties.

Figure 2 shows a schematic of a typical AFM instrument that consists of a cantilever-mounted tip, a Piezoelectric scanner, four position-sensitive photo detectors, a laser diode and a control unit. The process of operation of an AFM is relatively simple. The beam from the laser is directed against the back of the cantilever beam onto the quadrants of the photo detector. As the tip is moved across a sample, this causes the cantilever beam to bend or be twisted in manner that is proportional to the interaction force. This bending or twisting of the cantilever causes the position of the laser on the photo detector to be altered. The deflection of the cantilever beam can then be converted into a 3D topographical image of the sample surface (Gaboriaud and Dufrene, 2007; Kuznetsova et al., 2007; Lim et al., 2006).

Initially this technique was intended purely as a high-resolution imaging device, down to the sub-nanometre level (Alessandrini and Facci, 2005). However, it was soon adapted for measuring the interactive forces in a process known as force spectroscopy. In this process, the sample is moved towards the tip and then retracted, with the vertical displacement of the Piezoelectric scanner being recorded. This produces voltage data recorded by the photo detector as a function of the displacement of the Piezoelectric stage. A force curve can be produced from this which provides information about the interactions between the tip of the probe and the sample. This force data can be interpreted to

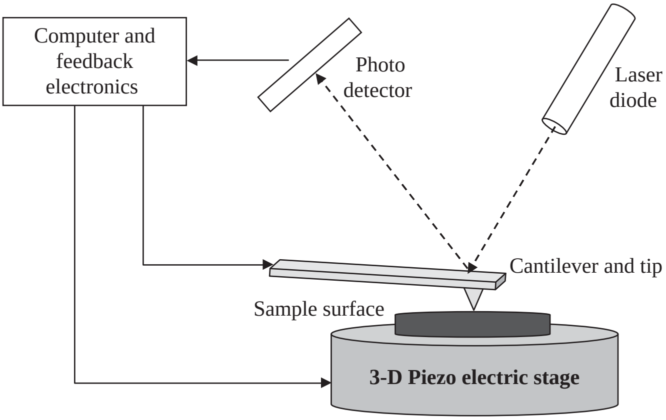

Figure 2 Schematic of an AFM setup.

allow information about the mechanical properties of the sample to be obtained. This method can be used to determine the effect of different cell materials on the mechanical properties of the cell wall. For example, this technique was employed by Touhami et al. (2003) to determine the Young's modulus of different areas of the Brewer's yeast cell wall (*Saccharomyces cerevisiae*). In their work, Touhami et al. (2003) found that a chitin bud scar had a Young's modulus value ten times higher than the value for the surrounding cell wall area.

Furthermore, a rigid glass bead can be glued to a tipless cantilever, and used as a force probe to compress single particles, such as Jurket T lymphomas cells (Lulevich et al., 2006) and polyelectrolyte microcapsules (Lulevich et al., 2003).

There are many related applications of AFM. For example, it has been used to determine the adhesive forces between *S. cerevisiae* cells and surfaces in biofilm formation, as well as many other organisms and non-biological particles (Bowen et al., 2001). An additional method has used AFM to detect local nanomechanical motion of the cell wall of *S. cerevisiae* caused by the active metabolic processes of the cell (Pelling et al., 2004). AFM has also been used to produce information on the conformational changes of single pyranose rings, which are one of the main monomer constituents of the yeast cell wall (Marszalek et al., 1998). In this work, the pyranose ring was identified as the unit controlling the molecular elasticity. This technique has the potential to elucidate the tensile properties of individual polymer chains of the polysaccharides that make up the yeast cell wall.

AFM has become an indispensable tool when investigating the forces associated with cellular and molecular biomechanical events. However, AFM does not currently have the ability to cause cell wall failure since it can only measure relatively small forces, in a range of nano- to micro-Newtons.

2.4 Optical trapping (also known as laser tweezers)

The optical trapping method uses a highly focused laser beam to trap and manipulate particles of interest in a medium (illustrated in Figure 3). The laser is focused on a dielectric particle (e.g., a silica microscopic bead), the refractive index of which is higher than the suspension medium. This produces a light pressure (or gradient force), which moves the particle towards the focal point of the beam, that is, the beam waist (Lim et al., 2006).

Optical trapping is a very sensitive method that is capable of the manipulation of sub-micron particles such as individual viruses and bacteria. Figure 4 is an illustration of the use of the optical trapping method to measure the elastic properties of RBCs (Mills et al., 2004).

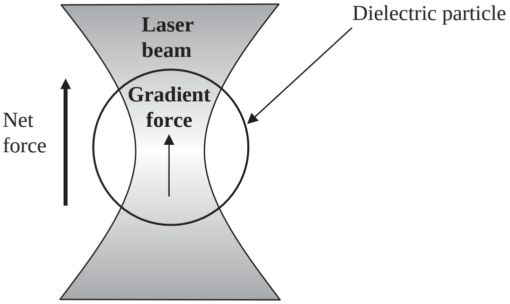

Figure 3 Optical trapping of a dielectric particle (simplified from Lim et al., 2006).

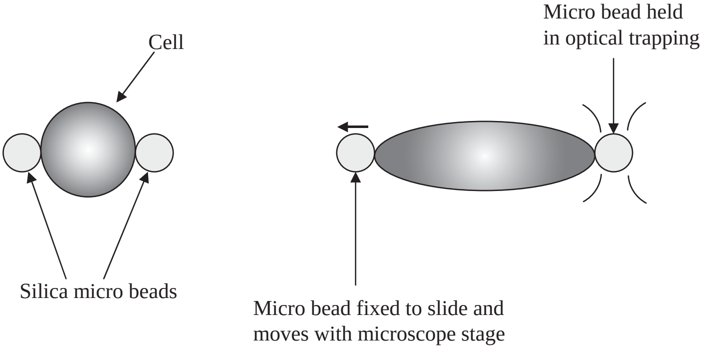

Figure 4 Stretching of a particle (e.g., a RBC) using the optical trapping method (modified from Mills et al., 2004).

Initially silica microbeads were attached to opposite sides of the cell with the bead on the left-hand side being attached to the surface of a glass slide and the right-hand bead held in the optical beam. The trapped bead remained stationary as the glass slide was moved to the left causing the cell to stretch. From this measurements of the stretching force of the cell could be determined.

There are numerous examples of the use of the optical trapping to gain insight into the mechanical properties of cells. As well as measuring the mechanical properties of RBCs, the stretching of DNA molecules has also been investigated (Bryant et al., 2003; Smith et al., 1996). A dual wavelength optical trapping method has also been described in which one beam was used to trap a *S. cerevisiae* (yeast) cell, whereas the other beam was used to generate Raman spectra (Creely et al., 2005). Raman spectroscopy produces an individual spectrum of the macromolecules within the cell and can observe changes occurring during cell replication. The budding of a yeast cell was observed for 150 min and biological changes in the cell were monitored. The use of optical trapping in this case prevented problems of fluorescence that have been previously reported for cells adhering to a glass slide (Xie and Li, 2003). As well as this, the optical trapping method has been used to make the first direct measurements of the Young's modulus of bacterial macrofibers of *Bacillus subtilis* (Mendelson et al., 2000).

One of the advantages of the optical trapping method is that there is limited physical contact with the cell, although it is possible that it could be damaged by the laser (Lim et al, 2006). In addition, it is possible to measure forces in the sub pico-Newton range, which is extremely difficult to do by other methods. However, these small forces mean that it is not appropriate for investigating the response of samples to large deformations, especially if the sample has a cell wall.

2.5 Diametrical compression (also called compression testing by micromanipulation)

2.5.1 Experimental setup

In this technique, an individual particle is compressed between two flat parallel surfaces, usually until it ruptures. By measuring the force being applied to the particle and the displacement of the surfaces, force-deformation data can be found. Figure 5 shows an illustration of a particle during compression where a force (F) is deforming it between two surfaces separated by a known distance ($2\bar{\eta}$).

Initial experiments using this method involved the compression of relatively large sea urchin eggs and visual measurement of the surface displacement to determine the cell deformation to the forces being imposed (Cole, 1932; Hiramoto, 1963; Yoneda, 1964, 1973). Recently, compression testing by micromanipulation was developed, which is capable of determining the mechanical properties of small cells or particles with sizes down to approximately 1 μm, employing forces of 1 μN or greater (Zhang et al., 1992a).

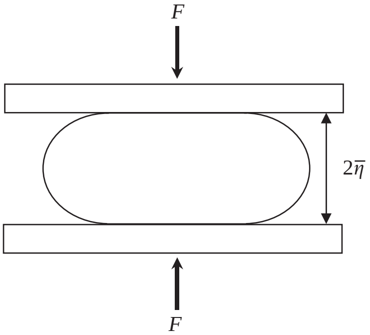

Figure 5 Compression experiment. Particle compressed by force F between surfaces separated by the distance $2\bar{\eta}$.

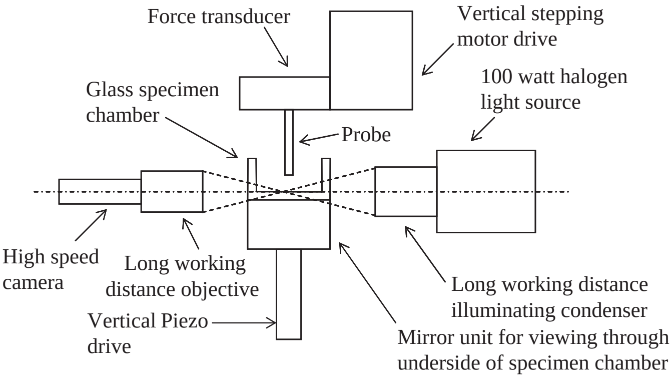

Figure 6 Schematic diagram of the newly built micromanipulation rig (reproduced from Wang et al., 2005). Permitted by Elsevier.

Figure 6 shows a diagrammatic representation of the most recent apparatus. In comparison with previous micromanipulation equipment (Blewett et al., 2000), the key feature of this rig is its capability of generating high-speed compressions using a Piezoelectric stack with a relatively large motion (of the order of 100 μm). In a recent study of the mechanics of tomato fruit cells (Wang et al., 2006a), compression speeds up to 1,500 $\mu m\,s^{-1}$ were used, although even higher speeds might have been achievable. The Piezoelectric stack is fixed on the base of the rig, and the glass chamber holding a suspension of the particles is mounted on top of the stack. The particles are actually compressed against the force transducer probe by upward displacement of the stack and chamber. This design also allows images of the particles to be obtained, viewing through the bottom and side. The other major modification from earlier equipment is the connection of a digital high-speed camera to the side view microscope, which in the work of Wang et al. (2005) allowed 510 × 484 pixel resolution images to be collected and recorded at 500 frames per second for later image analysis. The latter can be used to measure the extent of particle deformation and possibly changes in particle volume during compression and subsequent relaxation.

A range of experiments can be carried out using this micromanipulation equipment, for example, compression at different speeds, repeated compression, and loading and unloading. These allow the identification of elastic, viscoelastic and elastic-plastic properties. Figure 7 shows compression of an ion-exchange resin particle to different deformations, and then unloading. The corresponding force versus displacement data for loading and unloading are presented in Figure 8.

Figures 7 and 8 show this ion-exchange resin particle was very elastic up to a deformation of 46%. The contact radius and lateral extension of the particle were also measured as a function of time (data not shown),

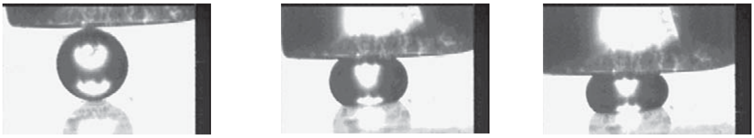

(a). Before compression (0%) (b). Loading (36%) (c). Final deformation (46%)

(d). Unloading (36%) (e). Totally released (0%)

Figure 7 Images of an ion-exchange resin particle (DOWEX 1X8-200, Sigma-Aldrich, UK) compressed to different deformations (values in brackets) and then released. The particle diameter was 163 μm (images provided by T. Liu, University of Birmingham, UK).

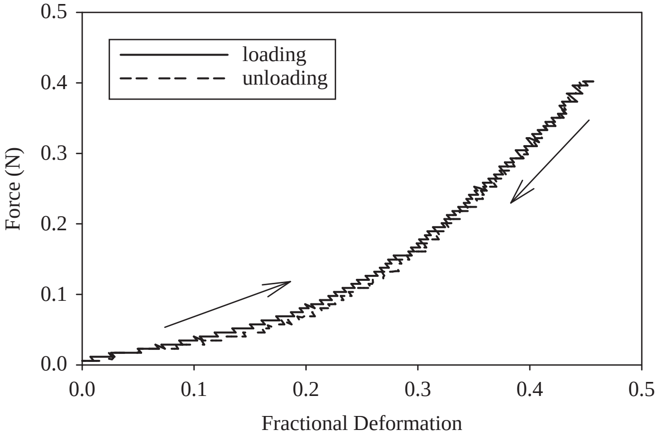

Figure 8 Loading and unloading curves for a single 163 μm diameter ion-exchange resin particle (DOWEX 1X8-200, Sigma-Aldrich, UK) obtained at a speed of 22.4 $\mu m\,s^{-1}$ (data provided by T. Liu).

and this information can be used for validation of later theoretical modelling of the deformation (see Section 2.5.2).

However, some particles, for example, single Eudragit microparticles, show significant hysteresis on loading and unloading, as shown in Figure 9 (Yap et al., 2008). The dotted line is the best fit to the loading data using the Hertz equation, which will be described later. Figure 9 also shows that the force dropped to zero before the displacement reduced to zero, which indicates the particle had undergone some plastic deformation.

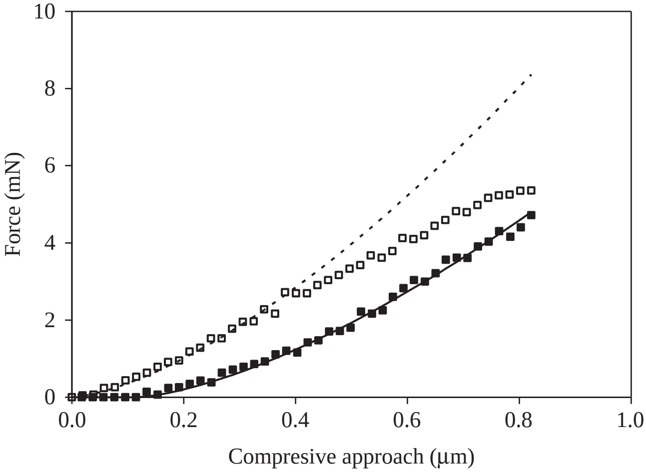

Figure 9 Typical loading (□) and unloading (■) data for a single Eudragit® L100-55 particle (Degussa Rohm, UK) compressed to a final strain of 6.0% (diameter = 27.4 μm) (Yap et al., 2008). Permitted by Elsevier.

Some particles can be viscoelastic or lose liquid under compression, for example, hydrogels and plant cells, and the force versus displacement data may therefore vary with the compression speed.

Force versus displacement data are directly useful in comparing some simple mechanical properties of particles from different samples, for example, the force required to break the particle and the deformation at breakage. However, these properties are not *intrinsic*, that is, they might depend on the particular method of measurement. Determination of intrinsic mechanical properties of the particles requires mathematical models to derive the stress–strain relationships of the material.

2.5.2 Mathematical modelling of the compression of single particles

2.5.2.1 Hertz model. The mechanics of a sphere made of a linear elastic material compressed between two flat rigid surfaces have been modelled for the case of small deformations, normally less then 10% strain (Hertz, 1882). Hertz theory provides a relationship between the force F and displacement h_p as follows:

$$F = \frac{4E\sqrt{R}}{3(1-v^2)}\left(\frac{h_p}{2}\right)^{\frac{3}{2}} = \frac{4}{3}\frac{\sqrt{R}}{2^{1.5}}E^* h_{p^{3/2}} \tag{1}$$

where R, E and v are the radius, Young's modulus and Poisson's ratio of the sphere, respectively. E^* is the reduced modulus:

$$E^* = \frac{E}{1-v^2} \tag{2}$$

which can be estimated by fitting Equation (1) to the experimental data using non-linear regression (see Figure 9). Hertz theory has been applied to describe data corresponding to small deformations of microparticles used for chromatography media (Müller et al., 2005). However, the applicability of Hertz theory is only to small displacements/strains and to linear elasticity (Tatara, 1991). At higher deformations, Tatara theory is more appropriate.

2.5.2.2 Tatara analysis. For larger deformations (up to 60%) of soft solid spheres made from linear and non-linear elastic materials, Tatara (1991, 1993) proposed a model to describe the relationship between the force and displacement. For the case of linear elasticity

$$h_p = \frac{3(1 - v^2)F}{2Ea} - \frac{2Ff(a)}{\pi E} \tag{3}$$

where a is the contact radius, given by

$$a = \left[\frac{3(1 - v^2)RF}{4E}\right]^{\frac{1}{3}} \tag{4}$$

$f(a)$ is given by

$$f(a) = \frac{2(1 + v)R^2}{\left(a^2 + 4R^2\right)^{3/2}} + \frac{1 - v^2}{\left(a^2 + 4R^2\right)^{1/2}} \tag{5}$$

Equation (3) reduces to Equation (1) if the second term on the right-hand side is ignored, which corrects the Hertz's displacement since Hertz's assumption of near sphericity is not valid at large deformations. For a given force, the displacement predicted by the Tatara model is always smaller than that from Hertz theory since the value of $f(a)$is positive.

From Equations (3)–(5), the relationship between the displacement and force can be determined if the values of R, E and v are known. In other words, if experimental data of force versus displacement are available, they can be used to determine the value of E given values of R and v.

The relationship between the force and displacement in the Tatara model (Equation (3)) may be approximated by a semi-empirical equation (Andrei et al., 1996):

$$F = c_1 {h_p}^{3/2} + c_2 {h_p}^3 + c_2 {h_p}^5 \tag{6}$$

where c_1 is equal to the coefficient of the Hertz equation:

$$c_1 = \frac{4E}{3(1 - \upsilon^2)} \frac{\sqrt{R}}{2^{1.5}} = \frac{4}{3} \frac{\sqrt{R}}{2^{1.5}} E^* \tag{7}$$

However c_2 and c_3 are arbitrary constants. Mathematically, Equation (6) may fit a given set of experimental data well since it has 3 adjustable constants, but the values of c_2 and c_3 are physically meaningless.

2.5.2.3 Viscoelastic model. Some microspheres may be viscoelastic or contain a large amount of liquid that can flow during slow compression or during force relaxation (during holding) after compression. In either case, they can show time-dependent behaviour, which may be described by a viscoelastic model. The simplest theoretical model of a viscoelastic solid is represented by a combination of a linear spring with a Kelvin–Voigt element (Haddad, 1995):

$$\sigma(t) = E_\infty \varepsilon_\infty \left(1 - \mathrm{e}^{-t/\tau}\right) + \sigma_0 \mathrm{e}^{-t/\tau} \tag{8}$$

where $\sigma(t)$ is the time-dependent stress, E_∞ and ε_∞ are, respectively, the Young's modulus and strain when the relaxation re-establishes equilibrium, σ_0 is the stress at time zero and τ the relaxation time. A more general and semi-empirical form of Equation (8), the so-called Maxwell model, which includes several exponential terms, is given by

$$\sigma(t) = \sigma_\infty + \sum_{i=1}^{n} \sigma_i \, \mathrm{e}^{-t/\tau_i} \tag{9}$$

where σ_∞ is the stress at the equilibrium, σ_i are proportionality constants and τ_i relaxation times.

In terms of force, a similar equation to Equation (9) can be written (Mattice et al., 2006) as

$$F(t) = F_\infty + \sum_{i=1}^{n} F_i \, \mathrm{e}^{-t/\tau_i} \tag{10}$$

where $F(t)$ is the time-dependent force, F_∞ the force when the relaxation reaches equilibrium and F_i are proportionality constants.

Mattice et al. (2006) extended Hertz analysis to spherical indentation of a viscoelastic material:

$$F(t) = \frac{4E\sqrt{R}}{3(1-\nu^2)} h_p^{3/2} = \frac{8}{3}\sqrt{R} h_p^{3/2} [2G(t)] \tag{11}$$

where the Poisson ratio ν equals 0.5 for an incompressible material and $G(t)$ is the shear relaxation modulus (Mattice et al., 2006). It was proposed that Equation (10) can be used to fit the force relaxation data from typical loading and holding experiments using compression testing, and that the shear relaxation modulus also relaxes with the same relaxation times as in Equation (10), so that

$$G(t) = K_0 + \sum_{i=1}^{n} K_i \, \mathrm{e}^{-t/\tau_i} \tag{12}$$

K_0 is related to F_∞ (Mattice et al., 2006) via

$$K_0 = \frac{F_\infty}{{h_{p\ \max}}^{3/2}\left(8\sqrt{R}/3\right)} \tag{13}$$

and

$$K_i = \frac{F_i}{(\mathrm{RCF}_i)\ {h_{p\ \max}}^{3/2}\left(8\sqrt{R}/3\right)}\ (i = 1,\ 2,\ 3,\ \ldots,\ n) \tag{14}$$

where RCF_i is called the "ramp correction factor" given by

$$\mathrm{RCF}_i = \frac{\tau_i}{t_R}\left[\mathrm{e}^{t_{R/\tau_i}} - 1\right] \quad (i = 1, 2, 3,\ \ldots,\ n) \tag{15}$$

where t_R is the time taken to compress the material. From the values of $K_0, K_1, K_2, \ldots, K_n$, the instantaneous shear modulus (G_0) and long-term shear modulus (G_∞) can be estimated.

$$G_0 = \frac{\sum\limits_{i=0}^{n} K_i}{2} \tag{16}$$

and

$$G_\infty = \frac{K_0}{2} \tag{17}$$

The corresponding Young's moduli are

$$E_0 = 2(1 + v)G_0 = 3G_0 \tag{18}$$

$$E_\infty = 2(1 + v)G_\infty = 3G_\infty \tag{19}$$

The theoretical force versus time relationship for loading may be given by the generalised Boltzmann integral expression (Mattice et al., 2006)

$$F(t) = \frac{8\sqrt{R}}{3}\int_0^t G(t-u)\left[\frac{d}{du}h_p^{3/2}(u)\right]du \tag{20}$$

The relationship between h and t is linear if the deflection of the compression probe due to its compliance is negligible, given by

$$h_p(t) = V_0 t \tag{21}$$

where V_0 is the moving speed of the probe.

Substituting Equations (10), (12) and (21) into (20) and integrating by parts gives

$$F(t) = 4\sqrt{R}\ {V_0}^{3/2}\left[\frac{2}{3}K_0 t^{3/2} + \sum_{i=1}^{n} K_i\ \mathrm{e}^{-t/\tau_i}{\tau_i}^{3/2}\left(\sqrt{\frac{t}{\tau_i}}\,\mathrm{e}^{t/\tau_i} - \int_0^{\sqrt{\frac{t}{\tau_i}}} \mathrm{e}^{x^2}dx\right)\right] \tag{22}$$

where $\int_0^{\sqrt{t/\tau_i}} e^{x^2} dx$ cannot be solved analytically, and has to be determined numerically.

It should be pointed out that Equation (11) should be modified to Equation (1) when compression of a single particle between two surfaces is modelled, that is, spherical indentation is replaced by compression between two surfaces. Applications in which these models were applied to experimental data from compression testing are described later.

2.5.2.4 Models to describe microparticles with a core/shell structure. Diametrical compression has been used to measure the mechanical response of many biological materials. A particular application has been cells, which may be considered to have a core/shell structure. However, until recently testing did not fully integrate experimental results and appropriate numerical models. Initial attempts to extract elastic modulus data from compression testing were based on measuring the contact area between the surface and the cell, the applied force and the principal radii of curvature at the point of contact (Cole, 1932; Hiramoto, 1963). From this it was possible to obtain elastic modulus and surface tension data. The major difficulty with this method was obtaining accurate measurements of the contact area.

Following on from this work two types of mathematical model were developed that do not rely on measuring the contact area. These models are the ''liquid-drop'' model (Yoneda, 1973) and the elastic membrane model (Cheng, 1987a; Feng and Yang, 1973; Lardner and Pujara, 1980).

The liquid-drop model was used to model the deformation of sea urchin eggs (Yoneda, 1973). This theory assumes that the tensions in the wall during the compression are uniform and isotropic as is stated by Cole (1932) and Yoneda (1964). However, Hiramoto (1963) suggested that the circumferential tensions are actually up to two times greater than the tensions in the meridian direction. This result suggests that the use of the liquid-drop model may not be appropriate to determine material properties of cells.

An analytical elastic membrane model was developed by Feng and Yang (1973) to model the compression of an inflated, non-linear elastic, spherical membrane between two parallel surfaces where the internal contents of the cell were taken to be a gas. This model was extended by Lardner and Pujara (1980) to represent the interior of the cell as an incompressible liquid. This latter assumption obviously makes the model more representative of biological cells. Importantly, this model also does not assume that the cell wall tensions are isotropic. The model is based on a choice of cell wall material constitutive relationships (e.g., linear-elastic, Mooney–Rivlin) and governing equations, which link the constitutive equations to the geometry of the cell during compression.

The constitutive equations relate the stresses and strains that are generated in the cell wall during the compression of a cell. Constitutive equations can be obtained by assuming that the cell wall is hyperelastic, in which case the stress components can be derived from a strain energy function. Strain energy is the energy stored in a body because of its elastic deformation, and is equal to the work required to produce the strain in the body. There are many choices of strain energy function that can be used depending on the cell wall material properties. In the case of Feng and Yang (1973), the constitutive equations were based on a Mooney–Rivlin model previously used to describe rubber material properties. On the other hand, Lardner and Pujara (1980) employed a Skalak–Tozeren–Zarda–Chien (STZC) material relationship. These relationships have been used to represent the material properties of RBCs and sea urchin eggs. Cheng (1987a) gave a generalised Hooke's law strain energy function, which allows various ways of deriving the strain energy function to be considered. The assumption of Hooke's law implies a linear relationship between the stress and the strain (i.e., a constant elastic modulus) although a non-linear force-deformation curve will be observed because of changes in the geometry of the cell as it is deformed. The generalised Hooke's law strain energy function may be written as an explicit function of the strain, but this requires that the definition of strain be considered carefully. In addition to this, the equations of Feng and Yang (1973) and Lardner and Pujara (1980) are expressed in terms of stretch ratios, which are a measure of deformation, and are often used for materials that can support high deformations before failure. Stretch ratios are defined as the length of a section in a given direction following deformation divided by its original length. Each strain measure also has a different relationship to the stretch ratio.

The elastic membrane model can be solved using a finite element approach (Cheng, 1987). The finite element approach has the advantage of being able to take into account irregularities such as non-spherical cells, local and geometric material differences (e.g., bud scars on the surface of yeast cells), assuming that detailed information is available about such irregularities. However, it is advisable to validate any finite element model against a corresponding analytical solution. As well as this, all but the most expert users treat the finite element model as a "black box" without fully understanding how the model results are generated.

The elastic membrane model assumes that the cell is a thin-walled sphere filled with incompressible fluid. Because the wall is thin, it may be treated as a mechanical membrane. It can be presumed that the wall cannot support out-of-plane shear stresses or bending moments. This situation is described as plane stress, as the only non-zero stresses are in the plane of the cell wall. Furthermore, the stresses can be expressed as

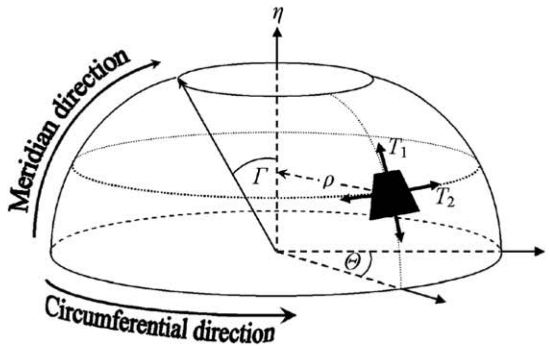

(a). Compound view

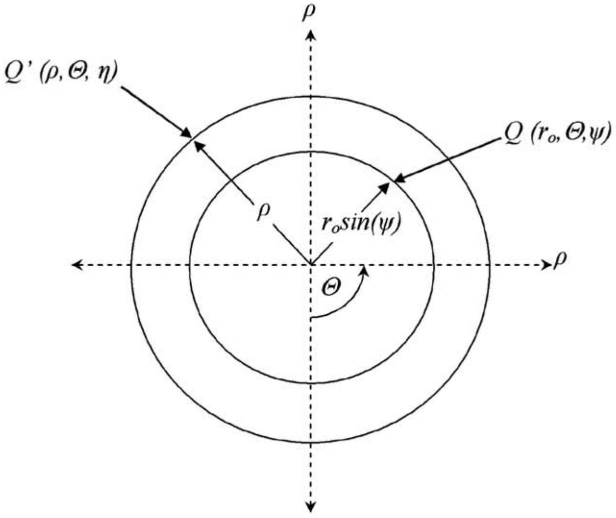

(b). Top view

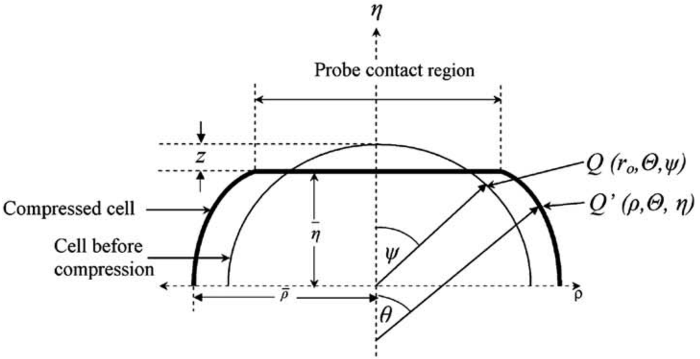

(c). Side view

wall tensions. It is usually assumed that a cell is inflated before compression (i.e., there is an initial pressure difference across its wall), but microcapsules are usually not initially inflated.

It is assumed that the cell is symmetrical across the equatorial plane and axi-symmetrical around the axis of compression, the η axis. This symmetry allows the compression of the cell to be fully represented by a 2D curve in the positive η and ρ axis. To understand the elastic membrane model, the geometry of the spherical cell under compression can be represented by Figure 10.

From Figure 10 there are two directions that need to be considered when deriving governing equations for the elastic membrane model, the meridian and the circumferential directions. In addition, there are separate groups of governing equations for the contact and non-contact regions of the cell during compression. The independent variable in these equations is ψ, which relates the position of any point on the boundary of the cell back to the original position of that point in the inflated but uncompressed cell.

The governing equations corrected from those presented by Lardner and Pujara (1980) are defined as

Contact region:

$$\frac{d\lambda_1}{d\psi} = -\frac{\lambda_1}{\lambda_2 \sin\psi}\left(\frac{f_3}{f_1}\right) - \left(\frac{\lambda_1 - \lambda_2 \cos\psi}{\sin\psi}\right)\left(\frac{f_2}{f_1}\right) \tag{23}$$

$$\frac{d\lambda_2}{d\psi} = \frac{\lambda_1 - \lambda_2 \cos\psi}{\sin\psi} \tag{24}$$

where f_1, f_2 and f_3 are functions of the principal tensions and are defined later.

Figure 10 Geometry of a thin-walled spherical cell under compression as represented by the elastic membrane model. (a) Compound view showing the upper half of the cell corresponding to the positive η axis of a cell under compression. T_1 and T_2 represent the tensions in the meridian and circumferential directions, respectively, Γ represents the angle between the positive η axis and the edge of the contact region, ρ is the horizontal coordinate, and Θ the angle of rotation in the circumferential direction. (b) Top view of a cell in compression where $Q(ro,\Theta,\psi)$ is a point on the inflated cell, $r_o\sin(\psi)$ the radius at point Q, and $Q'(\rho,\Theta,\eta)$ the corresponding point on the compressed cell. (c) Side view of the cell in compression where $\bar{\eta}$ is the distance between the compression surface and the equatorial plane, $\bar{\rho}$ the distance between the η axis and the edge of the cell on the equatorial plane, z is half the displacement of the probe, also termed compressive approach, ψ the angular position of the point measured from the η axis before compression and θ angle between the normal to the surface and the η axis following compression.

Non-contact region:

$$\frac{d\lambda_1}{d\psi} = \left(\frac{\delta\ \cos\psi - \omega\ \sin\psi}{\sin^2\ \psi}\right)\left(\frac{f_2}{f_1}\right) - \left(\frac{\omega}{\delta}\right)\left(\frac{f_3}{f_1}\right) \tag{25}$$

where

$$\delta = \lambda_2 \sin\psi \tag{26}$$

and

$$\omega = \frac{d\delta}{d\psi} \tag{27}$$

$$\frac{d\lambda_2}{d\psi} = \left(\frac{\omega \sin\psi - \delta \cos\psi}{\sin^2\psi}\right) \tag{28}$$

The turgor pressure (P) inside the cell can be related to ω using

$$\frac{d\omega}{d\psi} = \frac{d\lambda_1}{d\psi}\frac{\omega}{\lambda_1} + \frac{\left(\lambda_1^2 - \omega^2\right)}{\delta}\left(\frac{T_2}{T_1}\right) - \frac{\lambda_1\left(\lambda_1^2 - \omega^2\right)^{1/2} Pr_0}{T_1} \tag{29}$$

where r_0 is the uninflated radius of the cell. Equation (29) is used to link the deformation of the cell to the forces imposed through the internal pressure P.

The functions of the principal tensions in Equations (23) and (25) are defined as

$$f_1 = \frac{\partial T_1}{\partial \lambda_1} \tag{30a}$$

$$f_2 = \frac{\partial T_1}{\partial \lambda_2} \tag{30b}$$

and

$$f_3 = T_1 - T_2 \tag{30c}$$

where T_1 and T_2 are the tensions in the meridian and circumferential directions, respectively. Equations (30a–30c) link the geometry (Equations (23)–(29)) to the tensions, which depend on the constitutive equation of the cell wall material. Since the compression of the cell consists of axi-symmetric deformation, T_1 and T_2 are principal tensions, which are defined with respect to the current deformed shape of the cell.

For the analysis of experimental force-deformation data, it is necessary to use a suitable constitutive equation for the material under test. The constitutive equation relates the stresses and strains that are generated in the wall during compression, and therefore relates the tensions and stretch ratios. For example, Liu et al. (1996) used a Mooney–Rivlin constitutive equation to investigate the compression of polyurethane microcapsules and the functions f_1, f_2 and f_3 are produced in corrected form below.

$$f_1 = \frac{\partial T_1}{\partial \lambda_1} = 2hC_1\left(1 + \beta\lambda_2^2\right)\left(\frac{1}{\lambda_2} + \frac{3}{\lambda_1^4\lambda_2^3}\right) \tag{31a}$$

$$f_2 = \frac{\partial T_1}{\partial \lambda_2} = 2hC_1\left[\left(\frac{3}{\lambda_1^3\lambda_2^4} - \frac{\lambda_1}{\lambda_2^2}\right)\left(1 + \beta\lambda_2^2\right) + 2\beta\lambda_2\left(\frac{\lambda_1}{\lambda_2} - \frac{1}{\lambda_1^3\lambda_2^3}\right)\right] \tag{31b}$$

$$f_3 = T_1 - T_2 = 2hC_1\left[\frac{\lambda_1}{\lambda_2} - \frac{\lambda_2}{\lambda_1} - \beta\left(\frac{1}{\lambda_1^3\lambda_2} - \frac{1}{\lambda_1\lambda_2^3}\right)\right] \tag{31c}$$

where C_1 and C_2 are material constants, $\beta = C_2/C_1$, h is the cell wall thickness, λ_1 and λ_2 are the principal stretch ratios in the meridian and circumferential directions, respectively.

When using the generalised Hooke's law strain energy function there are a number of possible strain definitions that can be used depending on the situation. When material deformation is very small the infinitesimal strain approach is a valid approximation with the strain defined as

$$\varepsilon_i = (\lambda_i - 1) \tag{32}$$

where ε_i is the infinitesimal strain in the ith principal direction. In situations where the deformation of the material is greater then alternative strain definitions need to be considered. When deformation is non-infinitesimal, then the most common strain definition is Green strain defined as

$$E_i = \frac{1}{2}\left(\lambda_i^2 - 1\right) \tag{33}$$

where E_i is the Green strain in the ith principal direction. This strain measure is more appropriate for large deformations and large rotations. It is computationally convenient. However, when large deformation is accompanied by large strain then the most appropriate strain measure is the Hencky or true strain, which is defined as

$$H_i = \ln \lambda_i \tag{34}$$

where H_i is the Hencky strain in the ith principal direction. From this it is possible to define the functions f_1, f_2 and f_3 for the Hencky strain as

$$f_1 = \frac{\partial T_1}{\partial \lambda_1} = \frac{2Eh_o}{3\lambda_1^2\lambda_2}\left[2 - \ln\left(\lambda_1^2\lambda_2\right)\right] \tag{35a}$$

$$f_2 = \frac{\partial T_1}{\partial \lambda_2} = \frac{2Eh_o}{3\lambda_1\lambda_2^2}\left[1 - \ln\left(\lambda_1^2\lambda_2\right)\right] \tag{35b}$$

$$f_3 = T_1 - T_2 = \frac{2Eh_o}{3\lambda_1\lambda_2}\ln\left(\frac{\lambda_1}{\lambda_2}\right) \tag{35c}$$

where E is the elastic modulus, h_o the cell wall thickness and λ_1 and λ_2 are the principal stretch ratios in the meridian and circumferential directions, respectively.

The method for solving these equations was outlined by Wang et al. (2004) and Liu et al. (1996). The governing equations were solved by the Runge–Kutta method using the MATLAB ode45 solver (The MathWorks Inc., Cambridge, UK). The simulations can be solved as a series of static equilibrium problems as the cell wall material is considered to be time independent (i.e., negligible viscoelasticity). In each step of a simulation, the probe is displaced a set amount depending on the time length of each step and the speed of compression. This probe displacement compresses and deforms the cell a certain amount following which the pressure inside the cell is adjusted until a number of boundary conditions are met including a constant cell volume. The fluid contents of the cell are assumed to be incompressible and the cell wall is assumed to be impermeable. At the end of each step the volume of the cell is determined and the cell boundary co-ordinates ρ and η calculated. Once all of the boundary conditions have been satisfied corresponding values for the pressure (P) and the deformation ($\bar{\eta}$) are generated. From this force (F) and deformation (X) data can be obtained using the following equations:

$$F = PA_c \tag{36}$$

where P is the turgor pressure and A_c the contact area between the probe and the cell. The deformation of the cell is defined using

$$X = \frac{z}{r_o \lambda_s} = 1 - \frac{\bar{\eta}}{r_o \lambda_s} \tag{37}$$

where z is half the distance that the cell has been compressed (Figure 10c) and λ_s the initial stretch ratio of the cell.

The expressions in Equations (31a, 31b and 31c) provide the functions required to solve Equations (23)–(29), using the following boundary conditions (Liu et al., 1996):

$$\psi = 0,\ \lambda_1 = \lambda_2 = \lambda_0$$

$$\psi = \Gamma,\ \lambda_1(\text{contact region}) = \lambda_1(\text{non-contact region})$$

$$\psi = \Gamma, \lambda_2(\text{contact region}) = \lambda_2(\text{non-contact region})$$

$$\psi = \Gamma,\ \eta = \bar{\eta}$$

$$\psi = \Gamma, \eta' = 0 \text{ or } \omega = \lambda_1$$

$$\psi = \frac{\pi}{2},\ \omega = 0$$

where Γ identifies the angle of the points on the edge of the contact region between the compression surface and the cell (Figure 10a), η the horizontal coordinates and $\bar{\eta}$ the distance between the compression surface and the equatorial plane (Figure 10c).

Numerical simulations produce force-deformation data whose shape and magnitude is dependent on the initial parameters defined within the model, including the elastic modulus (E), the uninflated cell radius (r_o) and the initial stretch ratio (λ_s). Experimental data are fitted to these numerical simulations allowing intrinsic material properties to be derived.

Applications in which these models were applied to experimental data from compression testing are described later.

3. STATUS AND APPLICATIONS

3.1 Biological particles

3.1.1 Animal cells in suspension culture

Animal cells lack a cell wall and so are considered to be relatively weak in suspension cultures. There have been inconsistent reports concerning the mechanisms by which animal cells might be damaged in bioreactors and about the protective effects of medium additives (Michaels et al., 1991; Murhammer and Goochee, 1990), but it is now well-established that the predominant damaging mechanism in suspension cultures is bubble disengagement (Papoutsakis, 1991). To predict the breakage of animal cells in bioreactors or other processing equipment, it is necessary to know the intrinsic mechanical properties of the cells and the hydrodynamics of the process of interest. Intrinsic mechanical properties are independent of the method of measurement, and can be found by compression testing combined with appropriate mathematical modelling. Assuming the hydrodynamics are known, which is not always the case, and given some model of how the cells might distort and break in the flow, it should be possible to predict cell breakage in fluid flow. This has been demonstrated for disruption of animal cells in both laminar and turbulent flows (Born et al., 1992; Thomas et al., 1994), but it is yet to be shown that this approach would be successful in predicting cell damage caused by bubble disengagement.

Until recently there was only limited knowledge on the mechanical properties of animal cells. Micromanipulation has allowed some progress in this area. Figure 11 shows typical force-sampling time data for a hybridoma, with a bursting force of a few micro-Newtons. From such data the intrinsic mechanical properties of cell diameter, membrane tension at bursting and elastic area compressibility modulus can be

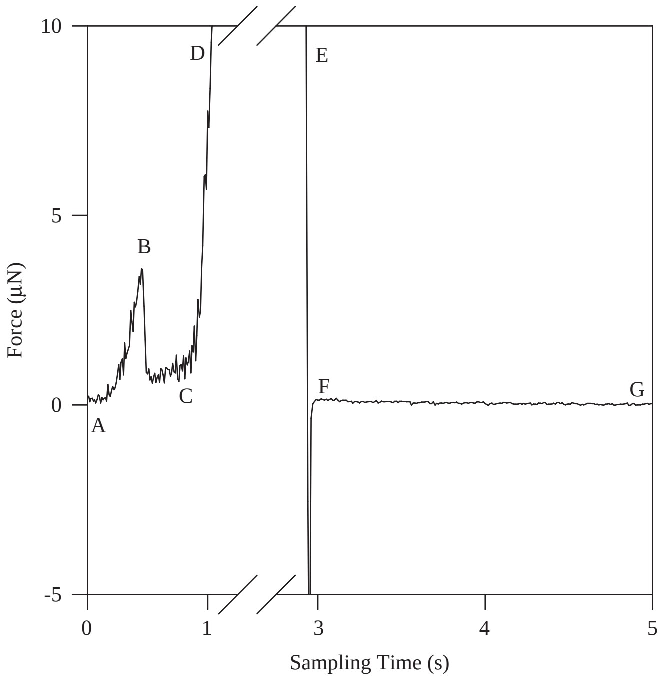

Figure 11 Typical force-sampling time curve for the compression of a TB/C3 murine hybridoma. (AB) cell compression, (B) cell bursting, (C) cell debris compression, (DE) probes touching each other and (FG) two probes separated (reproduced from Thomas et al., 2000). Permitted by Springer.

obtained (Zhang et al., 1992a). Micromanipulation has also been used to show how the culture additive Pluronic F68 can strengthen animal cell membranes (Zhang et al., 1992b), and to investigate the role of the plasma membrane, F-actin and microtubules in determining the mechanical properties of hybridomas (Welsh, 1998).

The mechanical properties of animal cells, including RBCs and leukocytes, have also been investigated using micropipette aspiration. Using this technique leukocytes are assumed to act as a liquid-drop leading to a surface tension of approximately $30\,\mathrm{pN}\,\mu\mathrm{m}^{-1}$ (Hochmuth, 2000). The mechanical properties of malaria-infected RBCs have been measured using the optical trap method (Lim et al., 2006). It was discovered that RBCs could be stiffened and its shear modulus increased by an order of magnitude after they were invaded by malaria parasite *Plasmodium falciparum*. This is interesting since there may be a relation between biomechanical states and the onset and progression of diseases such as cancer and malaria, and the cell mechanical properties may be used as an indicator of cellular diseases. A wide range of techniques has been used to investigate the mechanical properties of animal cells as only relatively small forces are required to deform these cell types. When cells that possess cell walls are of interest the number of applicable methods is not so wide.

3.1.2 Chondrocytes

Chondrocytes respond biologically to mechanical stimuli, and this is called mechanotransduction. Understanding cellular responses to mechanical stimuli and how they can be related to tissue level characteristics has many applications in biology, tissue engineering and medical science. Information about the mechanical properties of chondrocytes is fundamental to such research. Micropipette aspiration has been applied to investigate the deformation of single chondrocytes (Jones et al., 1999). It was found that human chondrocytes behave like viscoelastic solids. The Young's modulus of normal chondrocytes appeared to be very variable, but was of the order of 0.65 ± 0.63 kPa. However, the viscoelastic behaviour was not quantified.

Leipzig and Athanasiou (2005) designed a creep cytoindentation (i.e., cell poking) apparatus and applied a constant stress to adherent cells, while tracking the resulting cellular deformation using a cantilever. Middle/deep zone chondrocytes were isolated from articular cartilage, which was harvested from the distal metatarsal joint of one- to two-year-old heifers. The shape of the chondrocytes was approximated to be disc-like so that analytical data analyses could be made. Experimental data were fitted using three models. The linear elastic solid model gave a Young's modulus of 2.6 ± 0.8 kPa. The viscoelastic model (adapted from the Kelvin model described in Equation (8)) yielded an instantaneous modulus of 2.5 ± 0.8 kPa, a relaxed modulus of 1.5 ± 0.4 kPa and an apparent viscosity of 1.9 ± 1.8 kPa. Leipzig and Athanasiou (2005) also used a linear biphasic model to analyse the data, which was developed by Mow et al. (1980) to describe interstitial fluid flow-dependent viscoelastic responses of hydrated soft tissue, and obtained an aggregate modulus of 2.6 ± 0.9 kPa, a permeability of $2.6 \pm 3.1 \times 10^{-12}\,\mathrm{m^4\,N^{-1}\,s^{-1}}$ and a Poisson's ratio of 0.07 ± 0.02. However, direct measurement of the volume change of single cells gave a Poisson ratio of 0.26 ± 0.08 (Shieh and Athanasiou, 2006). Nevertheless, the three models seemed to give similar values of the Young's modulus. It was found that chondrocytes taken from the superficial zone were significant stiffer than those from middle/deep zone, which might be due to the different mechanical environments of the cells *in vivo*.

Chondrocytes surrounded by a layer of pericellular matrix (PCM) are called chondrons. Understanding the mechanical properties of the PCM is also important in investigating the biological responses of chondrocytes to mechanical stimulation since PCM determines the mechanical environment of the chondrocytes, and may serve as a transducer to amplify strains, while protecting the chondrocytes from damage. However, little data are available (Choi et al., 2007) and research is required in this area.

3.1.3 Yeast and bacterial cells

Yeast cells are generally considered less susceptible to mechanical damage due to the presence of a cell wall, which maintains the cell shape and provides protection from physical stresses (Klis et al., 2006). Baker's yeast cells (*S. cerevisiae*) have been widely used to produce many biological products. If these products cannot be engineered to be secreted from the cells, disruption is necessary to release the intracellular contents. A common unit operation for this purpose at industrial scale is high-pressure homogenisation (Middelberg, 1995). Modelling and optimisation of this process has been restrained by a lack of understanding of the mechanisms of cell breakage, which has arisen because of a lack of cell mechanical property information. However, Mashmoushy et al. (1998) demonstrated that such information could be obtained by compression testing by micromanipulation. Initially it was only possible to measure the bursting force of cells where a mean value of $101 \pm 2\,\mathrm{N}$ was measured from stationary phase Baker's yeast. The yeast cells were significantly stronger than hybridomas, presumably because of the presence of a cell wall.

A mathematical model was developed by Smith et al. (1998) to extract data on the elastic Young's modulus and some criteria of failure of stationary phase Baker's yeast from compression testing data. A mean Young's modulus of $150 \pm 15\,\mathrm{MPa}$ with a corresponding mean von Mises strain at failure of 0.75 ± 0.08 and a mean von Mises stress at failure of $70 \pm 4\,\mathrm{MPa}$ (Smith et al., 2000b) were obtained.

It was also shown by Smith et al. (2000a) that the bursting force was compression rate independent for speeds of 1.03–$7.68\,\mu\mathrm{m\,s^{-1}}$, which suggests little cell wall viscoelasticity or water loss from the cells during compression. However, separate squeeze-hold experiments using longer compression times have shown some relaxation does occur (Mashmoushy et al., 1998). Direct video measurements of cell volume might elucidate the reasons for this relaxation, although clear imaging of small yeast cells is yet to be achieved.

In homogenisation studies (Kleinig, 1997), it was discovered that larger cells were more susceptible to breakage, which suggested that the forces on these cells in the homogeniser were greater or that their ability to resist disruption was lower. This result supported the pressure gradient theory of cell disruption proposed by Kleinig (1997).

Besides compression testing, AFM has been used to derive intrinsic material properties of yeast cell walls by nano-indentation. This technique was employed by Touhami et al. (2003) to determine the

Young's modulus of different areas of the Brewer's yeast cell wall (*S. cerevisiae*). In this work, it was found that chitin bud scars had a Young's modulus of 6.1 ± 2.4 MPa, which is an order of magnitude higher than the value for the surrounding cell wall area of 0.6 ± 0.4 MPa. It is not entirely clear why these moduli are much lower than the global values found by Smith et al. (2000b), although it may be that nano-indentation by AFM gives surface-specific material properties.

The ability to derive the intrinsic mechanical properties of yeast cells should now allow the mechanisms of high-pressure homogenisation to be determined unambiguously, and *a priori* predictions of the extent of cell disruption to be made for given homogeniser conditions. This should allow better process optimisation.

Bacterial cells are generally much smaller than yeast cells, and are often not even approximately spherical. Figure 12 shows an *Escherichia coli* cell positioned beneath the end of a probe ready for compression. A typical force-deformation trace is given elsewhere, with a bursting force of approximately 4 μN (Shiu et al., 1999). Modelling compression data from such cells remains an unsolved challenge, and the poor quality of the images will probably prevent accurate, direct, volume estimations. Nevertheless, it may eventually be possible to produce intrinsic material properties from compression testing data and predict their breakage in high-pressure homogenisation.

In addition to using compression testing, the Young's modulus of bacterial macrofibers of *Bacillus subtilis* has been determined to be 50 MPa using the optical trap method (Mendelson et al., 2000).

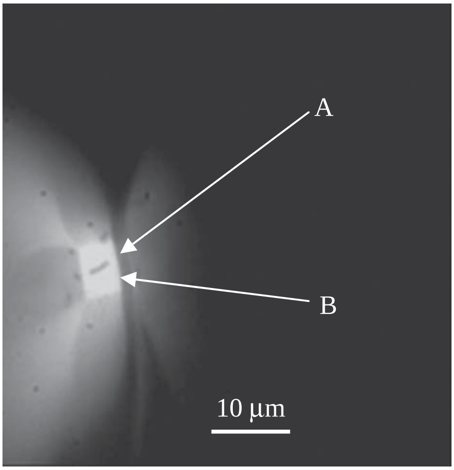

Figure 12 An *E. coli* cell positioned beneath the squared end of a probe ready for compression: (A) cell and (B) probe. Photograph by courtesy of C. Shiu. Permitted by Springer.

3.1.4 Filamentous microorganisms

By using glues, it is possible to attach a filamentous microorganism to two probes to allow it to be stretched by micromanipulation to breakage. Such a method was developed by a student of the authors (A. D. Roberts) and was used to determine directly the tensile strength of single fungal hyphae, specifically of *Fusarium graminearum*. Samples, which were taken from early and late stages of growth and from the stationary phase of a shake flask culture were tested both live, and after heat shock treatment (73°C for 10 min). Live hyphae were weakest (approximately 40 μN) during the late stages of growth, and strongest (approximately 70 μN) during the stationary phase. These forces correspond to Young's moduli for the wall materials of the order of 50–100 MPa, assuming linear elastic behaviour and assuming reasonable values for hyphal diameter and cell wall thickness. Heat-treated, single hyphae were significantly stronger (by approximately 8 μN) than those tested live. If this technique could be applied to other fungi, it might be possible to investigate the mechanisms of agitation damage to fungi in submerged cultures, for example, with antibiotic fermentations. However, many fungi are heavily aggregated in such cultures, and this might prevent unambiguous strength and strain measurements.

A similar technique has been used to investigate the elasticity and mechanical strength of the commercially important erythromycin-producing filamentous bacterium *Saccharopolyspora erythraea* where the mean Young's modulus was estimated to be 100 ± 20 MPa (Stocks and Thomas, 2001).

In addition to using the tensile test, the Young's moduli of filamentous microoganisms have also been determined using AFM to compress the wall, followed by mathematical modelling of the deformation using finite element analysis. For example, the Young's modulus of the cell wall of *Aspergillus nidulans* has been found from AFM testing to be 110–200 MPa (Zhao et al., 2005).

3.1.5 Plant cells

Compression testing by micromanipulation has been used to investigate the mechanical properties of tomato cells, both from suspension cultures and isolated single fruit cells.

In the case of suspension cultures, the mechanical properties of 2-week-old root callus cells of tomato (*Lycopersicon esculentum*) were investigated. These cells are approximately 70 μm in diameter, which allowed a clear side view of the compression to be recorded. Bursting forces were approximately 5 mN, at a compression rate of $23\,\mu\mathrm{m\,s^{-1}}$ (Blewett et al., 2000). However, squeeze-hold experiments show a relaxation of the holding force, with a time constant of the order of seconds (Figure 13). This is consistent with water loss from the cells,

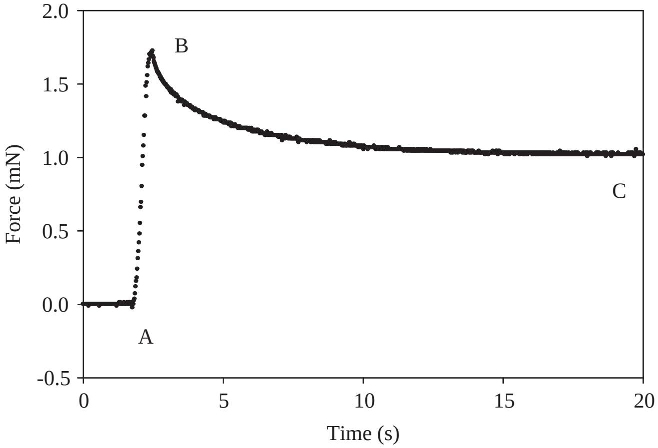

Figure 13 Force versus sampling time for compressing (curve AB) and holding (BC) a single tomato plant cell. The plant cell was 70 μm in diameter and was compressed at 23 μm s^{-1} (reproduced from Thomas et al., 2000). Permitted by Springer.

as expected from pressure probe experiments on other plant cells (Tomos, 2000). Image analysis has shown that water loss does occur (for the relaxation shown in Figure 13, approximately 2% of the volume at the beginning of the holding phase). Wang et al. (2006b) also used the pressure probe to determine the internal turgor pressure of suspension tomato cells. This technique was combined with compression testing to obtain independent turgor (hydrostatic) pressure measurements of cells, to show the pressure within a cell can indeed be found from Equation (29).

Data from compression testing of two-week-old suspension-cultured tomato cells at low strains has been modelled using the analytical elastic membrane model described earlier (Equations (35a)–(35c)). A mean elastic modulus of 2.3 ± 0.2 GPa was found (Wang et al., 2004). The cell wall was assumed *a priori* to be linear elastic in nature and the rate of compression was assumed to be sufficient for water loss from the cell during compression to be considered negligible. This result is significantly different to that found for single fruit tomato cells where Young's moduli of 30–80 MPa were obtained when applying the same assumptions (Wang et al., 2006a). It is not surprising that this difference exists between growing cells from culture and mature fruit cells.

As a single cell technique capable of achieving large deformations, the method complements the pressure probe method. It should be valuable in studies of how plant cell mechanical properties are affected by the molecular composition and structure of the wall, and how these are affected by food processing operations.

3.2 Biocompatible particles

Biocompatible microparticles (spheres or capsules) have been studied as carriers for entrapment of food (Gibbs et al., 1999), drugs (Aslani and Kennedy, 1996; Gonzalez-Rodriguez et al., 2002; Ribeiro et al., 1999), macromolecules (DeGroot and Neufeld, 2001; Kikuchi et al., 1997; Vandenberg et al., 2001) and cells (Read et al., 1999; Strand et al., 2000; Torre et al., 2000) or artificial organs (Chang, 1999). Microparticles for such applications should have not only the desired permeability but also adequate mechanical strength because they may be exposed to mechanical forces generated at the sites where they need to function, such as compression in cartilage and bone, tension in muscle and tendon, and shear forces in blood vessels. For example, microcapsules containing encapsulated islets, acting as an artificial pancreas, should have sufficient strength to prevent premature breakage in a patient’s body after implantation. Besides this, the release of active ingredients from microcapsules may also be triggered by mechanical signals (Kuen et al., 2001).

Alginate and chitosan are natural polysaccharides with excellent biocompatibility and biodegradability, and can form hydrogel or polyelectrolyte complexes under very mild conditions. In particular, water-soluble sodium alginate droplets can react with calcium chloride to form insoluble calcium alginate microspheres, which can be coated with a layer of chitosan. The mechanical properties of single calcium alginate microspheres can be characterised by diametrical compression. Microspheres bigger than 500 µm may be tested using commercial equipment, such as a texture analyser (Rehor et al., 2001). However, measurement of smaller microspheres can only be carried out using the micromanipulation-based compression testing described earlier.

Single calcium alginate microparticles with diameters of 20–60 µm were compressed at various speeds to a given deformation and held, or compressed to rupture. The forces corresponding to the deformations were measured by a force transducer (Zhao and Zhang, 2004). The force imposed on these particles increased when they were compressed, but relaxed significantly when they were held. For alginate microspheres, the faster the compression speed, the greater the imposed force for a given deformation. Calcium alginate microspheres coated with a shell of chitosan (called alginate–chitosan microcapsules with a shell thickness up to 11 µm) showed less force relaxation when they were held, compared with alginate microspheres. The thicker the shell, the less significant was the force relaxation exhibited by the microcapsules. The mean rupture force of alginate microspheres increased with compression speed, but in general this effect became less for alginate–chitosan microcapsules, and depended on the shell thickness. This is believed to result from the microspheres being the most permeable, with the permeability of the alginate–chitosan microcapsules decreasing with increasing shell thickness. However, the deformation at rupture was independent of the compression speed, which indicates it is not an elastic or viscoelastic parameter and may only be related to plastic failure. On average, the alginate–chitosan microcapsules were bigger than the alginate microspheres and had a greater rupture force.

To minimise speed-dependent behaviour, calcium alginate microspheres were tested at high speeds up to 1,000 $\mu m\,s^{-1}$, speeds that were achieved using a newly developed micromanipulation rig (Wang et al., 2005). High-speed video cameras also allowed measurement of changes in microsphere volume, caused by loss of liquid under compression. It was found that the reduction in microsphere volume was less than 10% for compression speeds of 800 $\mu m\,s^{-1}$ or higher. At lower speeds, or during relaxation on holding after compression, time-dependent phenomena became important. These phenomena have been modelled recently using finite element analysis based on the software package ABACUS (Nguyen et al., 2009). The force relaxation data were fitted by Equation (10) with $i = 2$, and it was found that the two relaxation times were $\tau_1 = 0.012\,s$ and $\tau_2 = 0.105\,s$. The values were used in subsequent modelling using ABACUS. Figure 14 shows a comparison of experimental force versus displacement/time data for compression and holding of single calcium–alginate microsphere with fitting by finite element analysis. As can be seen, there was a very good agreement, with regression coefficients all greater than 0.99. The model gave an instantaneous elastic modulus of E_0 of 450 kPa.

Modelling of the time-dependent phenomena may also be achieved using the viscoelastic model described in Equation (20). Figure 15 shows a typical force versus time curve for compression and holding of a calcium–shellac microsphere, compared with fitting by the model (Xue, 2008). The microsphere was produced by reaction of ammonium shellac solution with calcium chloride. The agreement can be seen to be very good. The instantaneous Young's modulus and long-time modulus were 1.56 and 0.54 MPa, respectively.

3.3 Non-biological particles

3.3.1 Microspheres

Non-biological microspheres are widely used in chemical, agrochemical, food, pharmaceutical and household products. Here two examples are described: microspheres used as chromatographic resins and pharmaceutical excipients used for tableting.

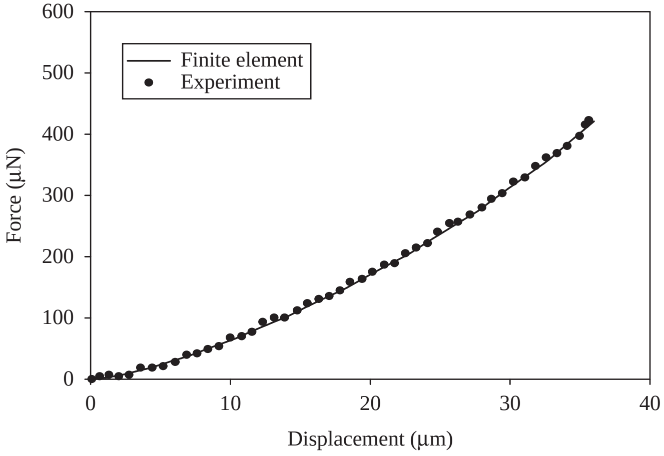

(a). Compression

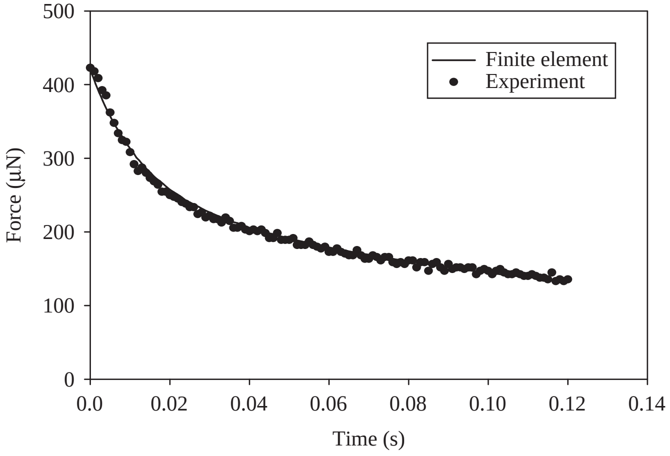

(b). Holding

Figure 14 Comparison of experimental force versus displacement/time data with fitting by ABACUS. The microsphere diameter was 125 µm and compression speed 800 µm s^{-1} (Nguyen et al., 2009). Permitted by Elsevier.

3.3.1.1 Chromatographic resins. Particulate chromatographic resins are additionally functionalised with ionic-, hydrophobic or affinity ligands, and can be used in downstream processing of biologics for purification of proteins and polynucleotides (Müller et al., 2005). These resins are mostly of polymeric nature and should have adequate caustic stability. The life-time of a chromatographic column, which partly depends on the mechanical stability of the resins, determines the overall processing costs to a great extent. Normally mechanically stable particles can be packed

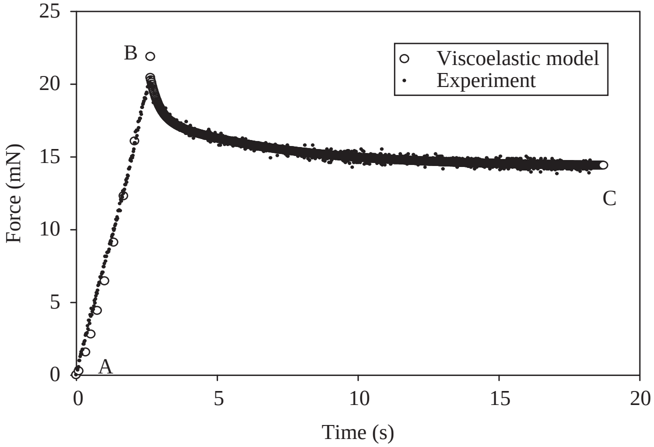

Figure 15 Comparison of force versus time data for compression of a calcium–shellac particle of 40 μm in diameter. The compression speed was $2\,\mu m\,s^{-1}$. Curve AB corresponds to compression and BC holding. The force relaxation data were fitted by Equation (10) with $i = 2$, $F_\infty = 14.3\ \mu N$, $F_1 = 8352\ \mu N$, $\tau_1 = 0.33$ s, $F_2 = 6.0\ \mu N$ and $\tau_2 = 4.5$ s (Xue, 2008).

into a column easily and do not shrink nor swell during chromatographic cycles. Understanding the mechanical properties of chromatographic particles is essential to successful design and operation of such processing equipment. The mechanical properties of single chromatographic particles may be related to their chemical composition and any surface modifications.

Using compression testing, ion exchange resins were shown to be elastic for deformations up to 46% (see Section 2.5.1). To determine the mechanical properties, Tatara's model (Tatara, 1991, 1993) was used to fit the compression data, assuming a material of non-linear properties. The fit is shown in Figure 16. As can be seen, there is a good agreement between the experimental data and fitting by the Tatara model.

Micromanipulation has also been used to determine the mechanical properties of methacrylate-based resins with different surface functionalities (Müller et al., 2005). The particle sizes ranged from 30 to 90 μm, depending on their chemical composition. It was found that the stiffness of the resins depended on the specific chemical modifications, and the difference was more pronounced in the dry state than in the wet state.

3.3.1.2 Pharmaceutical excipients. Pharmaceutical excipients in powders mixed with an active ingredient are often compacted into tablets as the final dosage form (Jivraj et al., 2000; Kotte and Rudnic, 1995; Rubinstein, 2000), and these tablets should have adequate mechanical

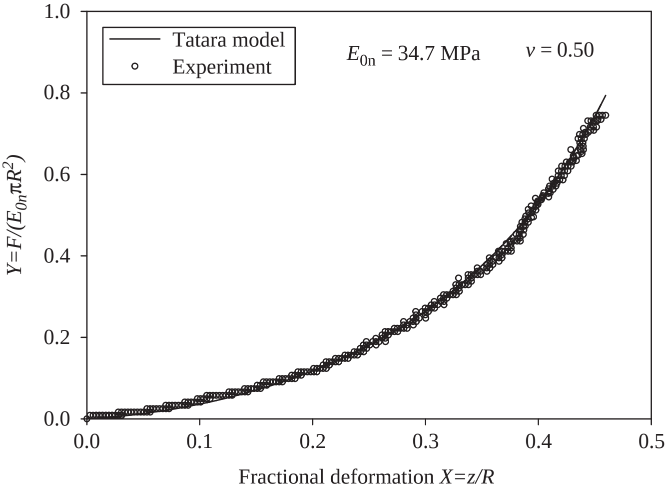

Figure 16 Comparison of the dimensionless force *Y* and fractional deformation of a single 163 μm diameter ion-exchange resin particle (DOWEX 1X8-200, Sigma-Aldrich, UK) obtained by diametrical compression and by numerical simulation using the Tatara non-linear elastic model. E_{0n} represents the initial Young's modulus at zero strain (data provided by Dr T. Liu).

strength to withstand the various handling operations in the logistic chain from producer to patient. Furthermore, a tablet should disintegrate and release the active ingredient to stomach or intestines at the right time in a reproducible manner (Kotte and Rudnic, 1995). To make rigid tablets, high-compaction pressures are often required. However, some of the active ingredients can be susceptible to high pressure and can be damaged by compaction. Therefore, it is important to understand the relationship between the mechanical properties of primary particles ($<100\,\mu$m) and their compaction behaviour, to produce tablets with adequate strength at the lowest compression pressure.

During compaction, primary particles are packed, re-arranged and can undergo deformation and possibly breakage. These events can occur sequentially or in parallel. The mechanical strength of a tablet may strongly depend on the mechanical properties of the primary particles and the particle–particle interactions within it. It is essential that the particles deform plastically or rupture since the stored elastic strains can weaken the tablet on release (Roberts and Rowe, 1987).

The mechanical strength of single microparticles relevant to pharmaceutical applications has been measured using compression testing by micromanipulation (Yap et al., 2006). Pharmaceutical excipients, comprising three enteric polymer particles Eudragit® L100-55, Eudragit® L100

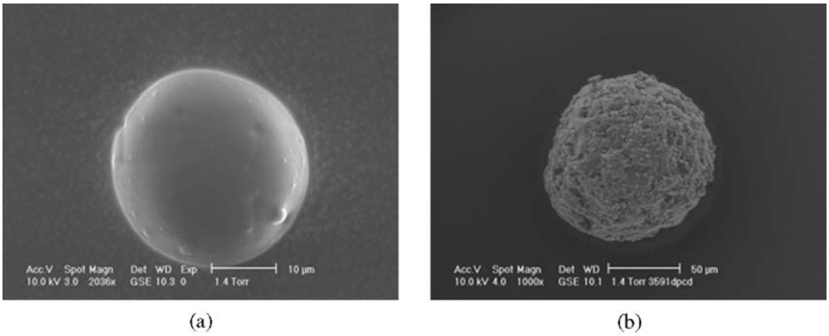

Figure 17 ESEM image of (a) Eudragit® L100-55 and (b) Advantose™ 100 (Yap et al., 2006). Permitted by Elsevier.

and Eudragit® S100 (Degussa Rohm, UK), and three different powders in the form of agglomerates, Advantose™ 100 (SPI Pharma, UK), Barcroft™ CS90 calcium carbonate (SPI Pharma, UK) and Starlac™ (Roquette, UK) were studied. Their diameters ranged from 20 to 90 µm. The enteric polymer particles and the agglomerates had distinct morphologies (Figure 17). The Eudragit® L100-55 particle exhibited a single rupture mode under compression by splitting into two roughly equal halves, as observed by a TV camera. A typical force versus compressive approach curve is presented in Figure 18a. However, particles of Advantose™ 100 showed a different mode of rupture. At the peak force, they split into many fragments. As shown in Figure 18b, there were a number of subsequent ruptures after the first major rupture.

Corresponding to small deformations of the particles, that is, within the elastic limit, the force versus displacement data were fitted by the Hertz model (Equation (1)), and the Young's moduli were determined to be 1.6 ± 0.2 GPa for Eudragit® L100-55 and 0.9 ± 0.4 GPa for Advantose™ 100 (Yap et al., 2006). Moreover, the hardness of a particle, H, could be obtained from the slope of the linear plastic region of the force-displacement curve at which it deviated from Hertzian behaviour, using the following relationship (Johnson, 1985):

$$F = 2\pi HRz \tag{38}$$

where F, R and z are the imposed force, particle diameter and compressive approach, respectively. The hardness was found to be 95 ± 14 MPa for Eudragit® L100-55 and 191 ± 15 MPa for Advantose™ 100 (Yap et al., 2008).

The same particles were compacted into a tablet using pressures up to 60 MPa (Yap et al., 2006), and pressure versus particle bed displacement data were obtained. It was found that the nominal rupture stress

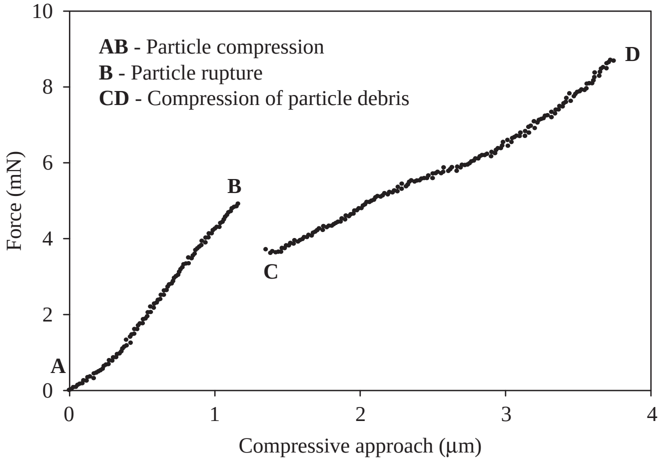

(a) Eudragit® L100-55 (Diameter = 20.0 μm)

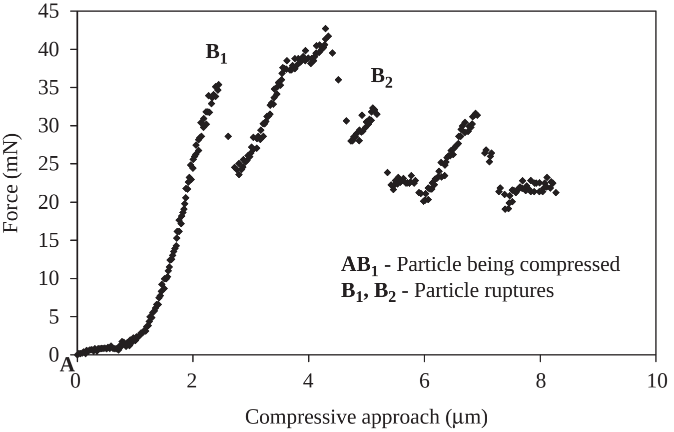

(b) Advantose^{TM} 100 (Diameter = 60.0μm)

Figure 18 Typical force-compressive approach relationship for the compression of a single particle to rupture (reproduced from Yap et al., 2006). Permitted by Elsevier.

(the ratio of the rupture force to the initial cross-sectional area) of the primary microparticles measured by compression testing was correlated with the compaction behaviour of the particles under confined uniaxial compaction. Single tablets were crushed using a Brazilian test, and scanning electron microscopy images of a crushed tablet were obtained (see Figure 19). As can be seen, the breakage occurred at the interface between feed particles, which implies that the crushing strength of the tablets was determined by the interfacial bonding rather than the mechanical properties of primary particles.

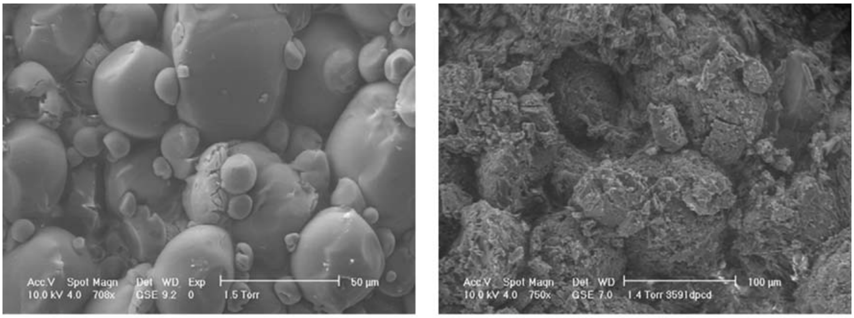

(a) (b)

Figure 19 Environmental SEM image of (a) Eudragit® L100-55 and (b) Advantose™ 100 tablet in the fracture region after diametrical compression (reproduced from Yap et al., 2006). Permitted by Elsevier.

3.3.2 Microcapsules

Capsules are basically particles with a core-shell structure, although the category also includes other structures, for example, spheres with an active ingredient embedded, a core with multiple shells, or a matrix with multiple embedded cores. Capsules for typical industrial applications can vary from several microns to millimetres in diameter, and these are usually called microcapsules. However, there is an increasing interest in preparing nanocapsules, of sizes less than one micron. Capsules containing active ingredients are widely used or have potential applications for producing household products (e.g., soaps, detergent and brighteners), personal care (health and beauty) products, printing and imaging products (carbonless copy paper, inks, toners, colorants), adhesives, sealants, paints, catalysts, antifouling agents and agrochemicals (herbicides, insecticides, fertilisers, repellents), in enhancing functions of food and feed (aromas and flavours, preservatives, nutrients, antioxidants), and in pharmaceutical and biomedical products to realise sustained (long lasting) drug delivery, vaccine delivery, gene therapy and active drug targeting (Arshady, 1999).

Active ingredients may be encapsulated by various processes, including *in situ* polymerisation, interfacial polymerisation, coacervation, spray drying, extrusion and fluidised bed coating (Madene et al., 2006). There are many different purposes of encapsulation, including stabilisation of an active ingredient, control of its release rate and conversion of a liquid formulation to solid. Capsules should have appropriate physical, mechanical and structural properties, possibly including particle size, size distribution, morphology, surface charge, wall thickness, mechanical strength, glass transition temperature and degree of crystallinity, flowability and permeability (Le Meste et al., 2002). Information about the mechanical properties of capsules is very important to understand their behaviour in different environments, including manufacturing processes and end-use applications. For example, capsules for most industrial applications should be strong enough to withstand the various mechanical forces generated in manufacturing processes, such as mixing, pumping and extrusion but may be required to be weak enough to release the encapsulated active ingredients by mechanical forces at end-use, such as the release of flavour by chewing. The mechanical strength of microcapsules and the release of their active ingredients, are related to microcapsule size, morphology, wall thickness, chemical composition and structure.

Direct methods of determining the mechanical properties of microcapsules include compression of a layer of them between two glass plates. Microcapsule mechanical strength has been characterised by the number of them being broken under a given weight applied to the top plate, but it was observed that the force was applied onto the largest microcapsules first, causing them to break, followed by the smaller ones (Ohtsubo et al., 1991). Although this method is practically useful, it conceals any difference in mechanical strength between microcapsules within a sample. Despite being more time consuming, results attained from assessment of single microcapsules is more accurate and reliable, and can give useful information about sample inhomogeneity (Schuldt and Hunkeler, 2000). Direct methods on single microcapsules include the use of a micropipette aspiration technique or an atomic force microscope probe to measure the elastic properties of single microcapsules. Unfortunately, the former technique cannot be used to determine the force required to rupture the microcapsules (Grigorescu et al., 2002), whereas the latter relies on compression of single microcapsules between a rigid spherical bead and a flat surface (Lulevich et al., 2006), which is difficult to implement. An uniaxial compression of single microcapsules has also been attempted by means of a texture analyser consisting of a penetrometer with a stress gauge (Edwards-Levy and Levy, 1999). This provided a measure of a particle's resistance to compressive force. However, assessment of single microcapsules was often impossible when the size was in the micron range (Martinsen et al., 1989). This limitation may be overcome by using compression testing by micromanipulation because this offers the capability to obtain force versus deformation data for single microcapsules as small as 1 μm, including to rupture.

The micromanipulation technique has been used to measure the mechanical strength of microcapsules of different size, shell thickness and shell composition (Sun and Zhang, 2001, 2002; Xue and Zhang, 2008; Zhao and Zhang, 2004; Zhang et al., 1999). For example, the mechanical properties of single melamine formaldehyde (MF) microcapsules with diameters of 1–12 μm were determined, including their viscoelastic and elastic-plastic properties (Sun and Zhang, 2001). It was found that the microcapsules were mainly elastic up to a deformation of $19 \pm 1\%$. Beyond this point, the microcapsules underwent plastic deformation and were ruptured at a deformation of $70 \pm 1\%$. However, the corresponding deformations at the yield point and at the rupture of urea–formaldehyde microcapsules were $17 \pm 1\%$ and $35 \pm 1\%$, respectively, which implies that urea–formaldehyde microcapsules were more brittle than those made of MF (Sun and Zhang, 2002). Besides the shell composition, the rupture strength of these microcapsules depended on their size and shell thickness. From compression measurements, the rupture force of different microcapsules can be compared by extracting information from a force-displacement curve up to rupture. The curves can also be fitted with equations derived from a theoretical model, for example, Lardner and Pujara's model (Lardner and Pujara, 1980; Liu et al., 1996). This approach has been used to determine intrinsic mechanical property parameters of microcapsule walls, for example, the Young's modulus, and in further mathematical modelling to determine viscous-elastic and plastic parameters where appropriate.

Liu et al. (1996) used Lardner and Pujara's model to estimate the Young's modulus of polyurethane microcapsules in a size range of 50–100 μm. Both neo-Hookean and non-linear elastic constitutive equations based on rubber-like Mooney–Rivlin materials were used to represent the stress–strain relationships, and it was found that the extensional rigidity of the microcapsule shell Eh (product of the Young's modules E and the shell thickness h) was approximately $540\,\mathrm{N\,m^{-1}}$ and the Young's modulus itself was 2.7 MPa, if the shell thickness was assumed to be 2 μm. However, the model could not be used to describe any plastic behaviour observed at large deformations. A similar approach has been taken to characterise the mechanical properties of urea formaldehyde microcapsules containing a self-healing liquid monomer dicyclopentadiene (DCPD) (Keller and Sottos, 2006). It was found that the mean microcapsule shell modulus was 3.7 ± 0.2 GPa, and this did not depend on whether the microcapsules were dry or immersed in the monomer. The microcapsules clearly showed plastic behaviour at large deformations, which was not modelled.

The mechanical properties of single hydrated dextran microcapsules ($<$ 10 μm in diameter) with an embedded model protein drug have also been measured by the micromanipulation technique, and the information obtained (such as the Young's modulus) was used to derive their average pore size based on a statistical rubber elasticity theory (Ward and Hadley, 1993) and furthermore to predict the protein release rate (Stenekes et al., 2000).

4. OTHER APPLICATIONS

4.1 Particle–particle adhesion

In industry, aggregates are often produced from aqueous solutions to aid processing or to form solid products. Examples of such operations include fermentation, flocculation, precipitation, suspension crystallisation and preparation of stable dispersions, for example, in the production of cement, china clay, paints and pigments (Shamlou and Titchener-Hooker, 1993). The mechanical stability of the aggregates, which is related to their mechanical strength, is a key factor in governing the success of such operations. Conceptually, the aggregate strength (e.g., the compressive or tensile strength) of an aggregate depends on the size and shape of the primary particles, the packing factor, inter-particle bonding strength, and the size, shape and porosity of the aggregate (Jiang and Logan, 1991). The porosity of an aggregate may be related to the packing factor, the shape factor and the fractal dimension of the aggregate, which may be quantified by image analysis, Coulter counting and laser scattering (Logan and Kilps, 1995; Tang et al., 2000; Zhang and Buffle, 1996). Consequently, information regarding the inter-particle bonding strength is crucial to understand the relationship between the properties of primary particles and those of the aggregates. Experimental techniques to characterise particle–particle adhesion include laser trapping (Sugimoto et al., 1997), micropipette aspiration (Fairbrother and Simmons, 1998; Fan et al., 2003; Yeung and Pelton, 1996) and micromanipulation (Fan et al., 2003; Willett et al., 1997).

The interactive force between two polystyrene particles of 2.13 μm in aqueous solution was measured using laser trapping by Sugimoto et al. (1997), who found that the force was a function of the separation distance between the two particles, in a good agreement with predictions by conventional DLVO theory (Castelain et al., 2008). The measured forces were of the order of several pico-Newtons.

The tensile strength of flocs formed by aggregating aqueous precipitated calcium carbonate sols with two water-soluble polymers has been measured by a micromechanical technique based on pulling apart single floc particles using two glass micropipettes (Yeung and Pelton, 1996), one of which worked as a cantilever. The stiffness of the cantilever had been pre-calibrated. The flocs had sizes ranging from 6 to 40 μm in equivalent diameter. Their primary particles were cigar-like in shape and had an average size of 1.34 μm. The tensile strengths ranged from 20 to 200 nN and showed no correlation with floc size. The tensile strengths were related to the fractal dimension and rupture behaviour of the flocs in processing equipment. A similar technique was adopted to measure liquid bridge forces between spherical agglomerates, and a model was developed to predict bridge rupture energies (Fairbrother and Simmons, 1998).

The interparticle forces induced by a liquid film layer between a pair of glass particles of near spherical shape has been measured by a micromanipulation technique (Willett et al., 1997). The two particles of 1.13 mm in diameter were glued to a force transducer probe and glass slide, respectively. The particles were coated with thin layers of silicone oils. The particles were first brought together until the particle surfaces just touched, followed by separation at a fixed velocity. A liquid bridge was formed between the particles. Complete traces of the force–separation relationship were achieved, and the interparticle forces were in very good agreement with a simple theoretical model based on the work of Adams and Perchard (1985).

Measurement of the adhesion between a pair of particles at temperatures from ambient to 580°C was carried out to understand particle processing in high-efficiency coal combustion systems, the integrated coal gasification combined cycle and pressured fluidized bed combustor systems (Masuda et al., 2004). In this work, the adhesive force between fly ash particles from a municipal solid waste incinerator was measured directly using micromanipulation, with the particles being heated on a hot stage under the microscope. The sizes of the coagulating particles ranged from 100 to several hundreds of microns. The results indicated that the adhesion increased with temperature. Moreover, the adhesive forces between particles taken from the incinerator were found to be significantly larger than those from biomass and coal combustors. Thermo-analysis and microscopic evidence suggested that the mechanism of the increasing adhesive force with temperature might be due to formation of liquid bridges at contact points between particles.

Interactions between micrometre-sized ice particles are interesting to researchers who study the preservation of frozen foods (Fan et al., 2003). Work in this area includes understanding the physical mechanisms of ice adhesion, measuring the adhesive strength of ice on surfaces and investigating new materials on which ice adhesion can be reduced. A micromanipulation apparatus similar to the one used for ash particles was used to measure the adhesive force between ice particles in air and sucrose solution. Ice particles were generated in the chamber of a heating/cooling stage under a microscope. The sizes of the ice particles ranged from 10 to several hundreds of microns. The adhesion forces between ice particles increased with their size and contact time, and the adhesion between ice particles in air was significantly stronger than that in sucrose solution. The findings were interpreted in terms of a simple model based on JKR theory (Johnson, 1985).

For completeness, it should be mentioned that laser trapping has been used to quantify the unbinding force between an actin filament and a single motor molecule of muscle (Nishizaka et al., 1995), the isometric forces generated by single kinesin molecules (Kuo and Sheetz, 1993) and the binding forces between *E. coli* bacterial adhesion and galabiose-functionalized beads (Fallman et al., 2003).

4.2 Particle adhesion to a surface

Understanding particle adhesion to a surface has applications in tissue engineering and particle processing. Experimental techniques for charactering particle adhesion to surfaces include laser trapping, AFM and microscopy with force measurement.

The interaction and attachment of human bone cells (human gingival fibroblasts and bone-forming human osteoblast cells) to different types of medical implant materials including glass, titanium and hydroxyapatite have been investigated to facilitate cell attachment and promote migration of progenitor cells to decrease healing times (Andersson et al., 2007). The cells were in contact with each surface for 30–120 s before they were pulled away using the optical trap. Twenty cells were tested on each surface type. It was found that most cells had an adhesion greater than 40–50 pN, exceeding the maximum force that could be measured. Some cells did not adhere, and no adhesive force could be detected. However, some cells had a relatively weak and measurable adhesive force in the range of 5–10 pN. Unfortunately, there was no significant difference in the force between different surfaces, or between the cell types. It seems the data were very scattered, and more cells should have been tested to give statistically representative results. A similar technique has been used to measure forces between a colloidal particle and a phospholipid bilayer (Sharp et al., 2006). Equilibrium and viscous force–distance profiles of silica microspheres of 1–5 μm in diameter on bilayers of dipalmitoyl phosphatidyl choline (DPPC) and on bare mica and DPPC monolayers under same electrolyte conditions were obtained, and they varied significantly with the bilayer.

AFM has been used to measure particle–surface interactions of lactose (Sindel and Zimmermann, 2001), which is a typical excipient for drugs formulated as solids. Information about the interaction forces between particles of crystalline lactose can help to understand and improve their flow properties. Owing to technical difficulties in handling a pair of particles, the interactions between a single particle of crystalline and a tablet of lactose were investigated, rather than studying a pair of particles. It was found that the average adhesion was in the order of 5 nN, which depended on the surface roughness and porosity of the particles. In addition, AFM allowed detailed scans of the substrate surface and could provide quantitative data about the surface roughness (Sindel and Zimmermann, 2001). AFM has also been used to measure the pull-off forces between glass microspheres and flat glass or silica surfaces, used as model systems for studying the behaviour of cohesive powders as a function of relative humidity (Jones et al., 2002). The glass and silicon substrates were treated with either a hydrophobic or a hydrophilic coating. It was found that for the hydrophilic surfaces the pull-off forces increased with relative humidity in the range of 5–90%, and depended on the roughness and asperity contacts at the interface. However, the pulling force did not change significantly with the relative humidity for hydrophobic glass. The results were explained by the theories of capillary bridge formation (Israelachvili, 1992), and could be used to interpret the behaviour of cohesive powders with different coatings or those which show a large humidity dependence (e.g., zeolites).

Recently, the adhesion of MF microparticles on a cellulose film in air as well as in liquid media was characterised using AFM. The cellulose film was made by dissolving cotton powder in *N*-methylmorpholine-*N*-oxide (NMMO) solution, followed by spinning on a silicon wafer. Spectroscopic ellipsometry was employed to measure the film thickness, and AFM was also utilised for characterising the film roughness and material distribution (Figure 20). The cotton cellulose film was also

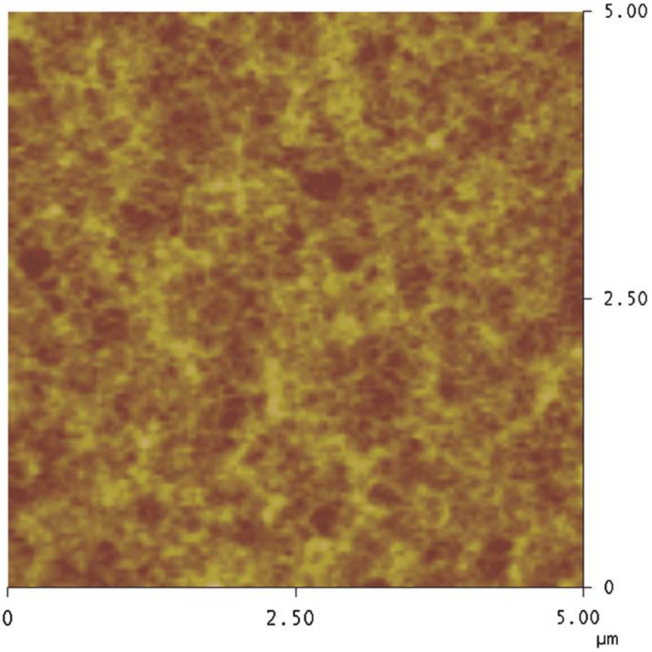

Figure 20 AFM image (tapping mode, height image) of a dry cellulose film. The cellulose concentration was 0.5%w/w. The root-mean-square surface roughness was 5.0 nm (courtesy of M. Liu, University of Birmingham, UK).

analysed with X-ray photoelectron spectroscopy (XPS) to make sure the film was free from residual solvent and confirm the presence of cotton material. It was found that the adhesion in air was in a range of 100–1,000 nN, whereas in water the adhesion was reduced to less than 4 nN.

Liu et al. (2002a, 2002b) developed a theoretical model to estimate adhesion energy between a microcapsule and a flat glass substrate, used as a model system to study cell–substrate interactions. It was found that the adhesion energy was related to the Young's modulus of the particle and the contact area. The Young's modulus of the microcapsule was determined independently by diametrical compression and analytical modelling based on a linear elastic model. The contact area of a urea formaldehyde microcapsule on a hydrophilic-fused silica substrate was measured using high-resolution reflection interference contrast microscopy and it was found that it increased with the osmotic pressure of the suspension liquid. This was due to a reduction in the microcapsule volume. The contact area did not change significantly with temperature in a range of 22–50°C when there was no phase transition of the capsule wall. The adhesion energy was in a range of 0.01–1.0 mJ m^{-2} depending on the osmotic pressure.

4.3 Fouling deposits on surfaces

4.3.1 Biomass and biofilms

Fouling of surfaces by biomass and biofilm formation is often detrimental, although in some cases it is encouraged, for example, for cell immobilisation in bioprocessing. Biofilm formation in industrial water systems can cause significant energy losses due to the increase in frictional resistance through the system, or cause microbial contamination in food processing. The biofilm usually consists of bacterial cells embedded in a network with tangled fibres of exopolysaccharides (EPS). Attachment of a fouling deposit to a substrate is termed adhesion, and molecular interactions within the deposit are defined as cohesion. Understanding the adhesive and cohesive properties of biofilms is crucial for effective control of biofilm growth or removal in industrial water systems, or in ensuring proper hygiene in food processing equipment.

To measure the adhesion strength of bacteria, it is necessary to remove them from the surface. Weiss (1961) measured bacterial adhesion by allowing cells to settle onto a glass surface of a sealed chamber, and then counting them with the aid of a microscope. After a period of incubation the chamber was turned upside down, the unattached cells fell from the surface and the remaining attached cells were recounted. This adhesion number method is purely observational, as it does not measure adhesion directly. Weiss also described a disc-shearing device, which employed a static disc with cells attached and a second disc spinning above the attached cells. The resulting shear stress was dependent on the rotation rate of the disc, the separation distance, the fluid velocity and the radial position. Christie et al. (1970) used a water jet impinged vertically onto the test surface at a fixed velocity to achieve similar ends. Since then there has been a number of modifications to such shearing techniques (Bryers, 1987). Recently, bacterial adhesion measurement has been improved by sophisticated techniques such as micromanipulation and AFM (Boyd et al., 2002; Chen et al., 1998). Micromanipulation can be used to characterise adhesion and cohesion of a layer of fouling deposit on substrate, whereas AFM is very powerful in measuring single cell-substrate adhesion.

Using micromanipulation, a technique has been developed to measure the mechanical properties, including the adhesive strength, of *Pseudomonas fluorescens* biofilms grown in pipe flows (Chen et al., 1998). A T-shaped probe was specially designed to pull the biofilms away from the inner surface of a pipe to which they were attached. The adhesive strength between a biofilm and the substratum was defined as the work required per unit area to remove the biofilm. It was seen that the bioflims exhibited viscoelastic behaviour. The adhesive strength was found to depend on the conditions under which the biofilm was grown. Increases in the fluid velocity, the concentration of suspended cells and the roughness of the attached surfaces resulted in greater biofilm adhesion, whereas pH did not appear to have any significant effect (Chen et al., 2005).

This technique was also used to assess the adhesive integrity of immobilised bacterial populations (biomass) of *P. fluorescens*, harvested at different growth times and then placed on a stainless steel substrate (Garrett et al., 2008). Each sample was tested in a flow chamber. After the biomass was exposed to the flow for a specific period, the sample was removed from the chamber and the apparent adhesion of the remaining biomass was measured using micromanipulation. The surface area of the substrate covered by the biomass was monitored by a digital camera and quantified by image analysis (Garrett et al., 2008). The results indicated a strong correlation between micromanipulation measurements of the adhesive strength and these flow chamber experiments. Both showed that the apparent adhesive strength of the biomass harvested from a given volume of cell suspension increased with growth time, which may be attributed to the increase in viable cell number. Moreover, the cohesive strength of the biomass was also characterised by measuring the force required to break the biomass layer by layer (Garrett et al., 2008). It was found that the apparent adhesive strength was greater than the cohesive strength. This implies that in cleaning by fluid flow or similar processes, the biomass would be removed from the top layer downwards. This has been validated by observations in the flow chamber. In general, the biomass adhesion onto a substrate was found to be much weaker than biofilm adhesion, suggesting a reduced presence of EPS in the biomass. Using these techniques, specific mechanisms of biomass detachment from a surface and optimised cleaning strategies may be tested.

The data produced using micromanipulation can be compared with data acquired using alternative techniques such as AFM and the flow techniques. These techniques complement each other by broadening the measurement range of the forces required to remove biomass/biofilm of different scales, that is, from single bacteria to a layer of fouling deposit. For example, micromanipulation can measure forces within the micro-Newton range, which is relevant to removal of a layer of deposit from substrate, whereas AFM can measure forces within the nano-Newton range, relevant to single cells. Flow cell techniques can be used to observe the mechanical and cohesive properties of biofilms, but cannot be used to measure directly the forces required to remove biomass/biofilms from a surface. As micromanipulation allows the measurement of adhesive and cohesive properties of biofilms directly, it is hoped that this technique can be used to fill the gap left by the limitations of AFM and flow cell devices.

4.3.2 Food fouling deposits

Food process plant rapidly becomes fouled with deposits on the interior surfaces of process equipment (Wilson et al., 2002). This may be caused by crystallisation of insoluble components, such as calcium phosphate in ultra-high-temperature milk fouling, reaction, for example, the polymerisation of β-lactoglobulin in milk or gelation of starch, and the growth of biofilms (Watkinson et al., 2004). Fouling deposits lower process efficiency through increased pressure drop and decreased heat transfer, and endanger both food quality and safety through potential product contamination. The problem of fouling is widespread. Consequently, cleaning-in-place (CIP) is a ubiquitous operation within the food industry, in which cleaning chemicals (e.g. up to 2% NaOH) followed by rinsing water are circulated, at temperature up to 70°C and high flow rate. This is expensive in time and has a tremendous environmental impact. Moreover, cleaning protocols are empirical and rarely optimised.

The micromanipulation technique of Chen et al. (1998) for measuring the adhesive strength of biofilms has been modified by Liu et al. (2002c) and used to measure the force required to remove food deposits from surfaces of stainless steel. Four model food systems were used, that is, tomato and dough representing starchy materials, and whey and egg proteins (Liu et al., 2007). Using micromanipulation, the adhesive strength of deposits that have been immersed in a cleaning chemical or water can be monitored. The force required to disrupt and remove the deposit (usually in the range of 2–10 $\mathrm{J\,m^{-2}}$) can be measured directly.

The effect of process variables such as temperature, time and chemical concentration has been determined in such studies, and the forces and the balance between cohesion and adhesion can be directly related to the ways in which surfaces are cleaned. For example, tomato deposits appeared to be largely cohesive in that the force to break the deposit in half exceeded that for total removal. It would seem that cleaning in this case occurs by removal of deposits by shear stresses overcoming the forces between the deposit and the surface (Liu et al., 2002c). However, milk protein deposits appeared largely adhesive and the force required to remove the deposits increased with thickness. Here, cohesive forces between elements of deposit were weaker than adhesive force between the deposit and surface, and cleaning occurred by breakdown of deposit cohesion (Liu et al., 2006a). These results are in agreement with those from liquid jets (Chew et al., 2004).

The adhesive strength of a food fouling deposit may be related to the surface free energy of the substrate. Zhao et al. (2004) have developed a theory that gives the minimum adhesion energy between a deposit and a surface:

$$\sqrt{\gamma_{\text{surface}}^{\text{LW}}} = \left(\frac{1}{2}\right)\left(\sqrt{\gamma_{\text{foulant}}^{\text{LW}}} + \sqrt{\gamma_{\text{fluid}}^{\text{LW}}}\right) \tag{39}$$

where $\gamma_{\text{surface}}^{\text{LW}}$, $\gamma_{\text{foulant}}^{\text{LW}}$ and $\gamma_{\text{fluid}}^{\text{LW}}$ are the Lifshitz–van der Waals surface free energies of the surface, foulant and fluid (e.g. water), respectively. Liu et al. (2006b) demonstrated that such a minimum adhesive strength (measured by micromanipulation) did exist for tomato paste deposits, at around $25\,\text{mN}\,\text{m}^{-1}$ predicted from Equation (39). However, the greater the thickness of the deposit, the greater the apparent adhesive strength and the lesser the apparent effect of the surface. The results indicate that cleaning depends on both adhesion between a deposit and surface and cohesion between its elements. This work may lead to increased food safety by improving and ensuring cleaning efficiency, minimising environmental impact by reducing the amount and concentration of effluents, and increased manufacturing efficiency through extensions of run length and minimisation of cleaning times.

4.4 Nanomanipulation of sub-micron/nanoparticles

Nanoparticles have numerous applications in the chemical, food, pharmaceutical, biomedical and semiconductor industries. For example, nanoparticles as drug carriers can increase drug efficacy, and can reduce toxicity and side effect after parenteral administration (Feng et al., 2002). Nanoparticles used for industrial applications should have desirable physical properties, including appropriate size, surface charge, surface area, porosity and mechanical strength. The functionality of nanoparticles, such as those used for drug delivery, may strongly depend on their mechanical properties. This has been demonstrated for hydrated dextran microspheres loaded with the model compounds myoglobin, ovalbumin, BSA and IgG. The (pseudo-)Young's modulus was correlated directly to the pore size of the particles and the release rate of the model drugs (Stenekes et al., 2000). In addition, it has been reported that controlled drug delivery from polymer carriers can be triggered by mechanical signals (Lee et al., 2001). Understanding the mechanical properties of single nanoparticles is essential to such applications.

To characterise the mechanical properties of a single nanoparticle requires the simultaneous determination of the force exerted on it and its deformation. This allows stress–strain relationships to be determined by modelling. Electron microscopy can be used to examine the surface morphology and structure of nanoparticles. Over the past few years, various tools have been developed for three-dimensional handling, assembly, characterisation and testing of fundamental building blocks like nanotubes and nanowires in scanning electron microscopes (SEMs), which include nanopositioning, nanomanipulation and microgripping devices (Eichhorn et al., 2007; Fahlbusch et al., 2005; Nakabayashi and Silva, 2007), but these devices did not have the capability to do force measurements. There have also been attempts to construct a manipulation device with a force sensor inside the chamber of an SEM (Yu et al., 1999) and an environmental scanning electron microscope (ESEM). Pioneering work on measuring the mechanical properties of materials in an ESEM includes *in situ* mechanical testing of fully hydrated carrots (Thiel and Donald, 1998), dry and hydrated breadcrumbs (Stokes and Donald, 2000), and the deformation of elementary flax fibres (Bos and Donald, 1999). However, in all these cases the samples were still relatively large, sometimes of the order of mm. A similar approach has been used for measurement of the fracture resistance of other brittle materials (Sorensen et al., 2001), but again the specimens were large.

Recently, an ESEM-based technique has been developed for characterising the mechanical properties of single nanoparticles by constructing and assembling a nanomanipulation device with a force probe in the chamber of an ESEM. This was used to demonstrate the feasibility of measuring the force required to compress single particles to a given deformation to infer their mechanical property parameters (Liu et al., 2005; Ren et al., 2007). This new nanomanipulation technique was first validated by comparison with a well established micromanipulation technique (Sun and Zhang, 2001) using both techniques to measure the force required to cause different deformations of single Eudragit microparticles. The validated nanomanipulation technique was then used to determine the mechanical properties of single polymethylmethacrylate (PMMA) nanoparticles. The technique has been

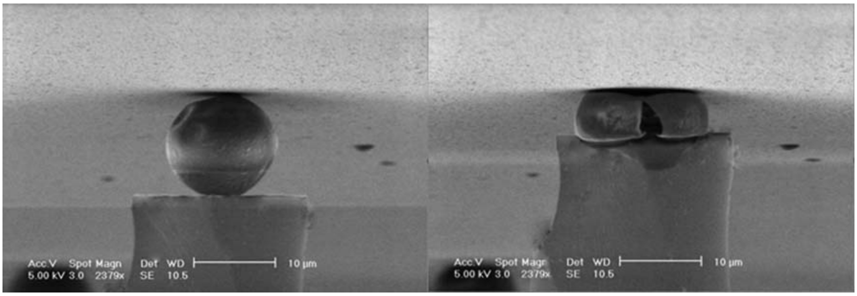

Figure 21 Images of a MF microcapsule before and after it was compressed to rupture under HV of ESEM: 5 kV, spot size 4. The microcapsule diameter was 16.5 µm (Ren et al., 2007). Permitted by Maney.

applied to determine the rupture mode of single melamine formaldehyde microcapsules under compression (Figure 21).

Very recently, *in situ* measurements of mechanical properties of individual W303 wild-type yeast cells have been made using an nanomanipulation system with an AFM cantilever probe (spring constant $0.02\,\mathrm{N\,m^{-1}}$) integrated into the chamber of an ESEM (Ahmad et al., 2007). Single cells were penetrated under two different conditions, that is, ESEM (600 Pa) and high vacuum (HV, approximately 3 MPa) modes. Data show that the penetration forces under HV conditions were approximately 25 times those under the ESEM mode, that is, 4 µN rather than approximately 150 nN for a cell size of 5 µm, with a penetration distance of 1 µm. The corresponding Young's moduli were estimated to be 2.2 ± 1.2 MPa under the ESEM mode and 21 ± 2 MPa under the HV mode, both based on the Hertz model. This work demonstrates that the apparent mechanical properties of the cells strongly depended on the environmental conditions within the microscope.

Although SEMs or ESEMs are very powerful in imaging nanoscale materials or particles, caution should be taken to avoid electron beam damage to specimen. This is particularly important when a nanomanipulation system with a force measurement device is to be used to characterise the mechanical properties of particles. Ren et al. (2007, 2008) identified that such damage depended on the electron dose and exposure time, as well as the type of materials under test, and it is extremely important to find a time window in which the damage is negligible to obtain reliable mechanical property data.

5. PERSPECTIVES ON FUTURE DEVELOPMENT

A number of micromanipulation-based techniques have been developed and used to measure the mechanical strength of single particles, particle–particle interactions, particle–surface or film–surface interactions, which have been biological or non-biological in nature. Although it is powerful, micromanipulation is very technically demanding, time consuming and not easy to use. Semi- or full automation of micromanipulation equipment should enhance its popularity. The data obtained directly by micromanipulation are very useful in terms of understanding how the properties vary with morphology, structure and chemical composition of the particles or the surface involved. Analytical models or finite element analyses are available to extract intrinsic elastic property parameters of particles with relatively simple structures (e.g., spherical microspheres, capsules or cells). However, there has been no adequate modelling of the plastic deformation of such particles. For particles with more complex structures such as multiple shells, or several particles embedded in a single carrier, analytical modelling may well be too difficult or impossible, and this is where finite element analysis can and will play an increasingly important role.

Both biological and non-biological particles are often exposed to mechanical forces in processing equipment. Understanding and predicting deformation and breakage of particles in such equipment is important to improve process design and operation. However, although understanding the mechanical properties of the particles is essential, modelling of the interactions between the particles and fluid or other particles is also required. So far, there has only been limited work on such modelling.

One of the challenges to chemical engineers in the 21st century is to produce functional products to meet ever increasing demands for consumer care and healthcare, which requires formulation of particulate products with multiphases and complex structures with scales from micro to nanometres. Mechanical characterisation of particles at sub-micro scale is likely to become more and more important, and this will require miniaturisation of micro/nanomanipulation devices, force sensors and the development of affordable electron microscopes. For healthcare, research on biomaterials, tissue engineering and stem cells and engineering–life interface will also require mechanical characterisation, in these cases of cells or biomaterials in their native state. This is difficult to achieve using existing electron microscopes because of beam damage (Ren et al., 2007, 2008). Ingenious solutions are required here, if the direct measurement of the mechanical properties of any and all micro to nanometre-sized particles is going to become a routine tool in research and process development.

NOMENCLATURE

a	contact radius (Equation (3)) (m)
c_1	equal to the coefficient of the Hertz equation (Equation (1))

c_2, c_3	arbitrary constants
f_1, f_2, f_3	functions of the principal tensions defined in Equations (30a)–(30c) ($\mathrm{N\,m^{-1}}$)
h	cell wall thickness during compression (m)
h_0	initial (uninflated) cell wall thickness (m)
h_p	displacement (m)
h_pmax	maximum displacement (m)
$h_\mathrm{p}(t)$	time-dependent displacement (m)
r_0	uninflated cell radius (m)
t	time (s)
t_R	time taken to compress a particle (Equation (15)) (s)
u	arbitrary time variable (Equation (20)) (s)
x	arbitrary variable (Equation (22))
z	half the displacement of the probe, also termed compressive approach (m)
A_c	contact area between the probe and the cell (Equation (32)) ($\mathrm{m^2}$)
C_1, C_2	material constants in the Mooney–Rivlin (1940) strain energy function (Pa)
E	Young's or elastic modulus (Pa)
E_0	instantaneous Young's modulus corresponding to G_0 (Equation (18)) (Pa)
E_{0n}	initial Young's modulus for non-linear elastic material (Pa)
E_i	principal component of Green strain in direction i
E^*	reduced modulus (Pa)
E_∞	long-term Young's modulus corresponding to G_∞ (Equations (8) and (19)) (Pa)
F	force on particle (N)
$F(t)$	time-dependent force (N)
F_i	proportionality constants (N)
F_∞	force when the relaxation re-establishes equilibrium (N)
$G(t)$	shear relaxation modulus (Pa)
G_0	instantaneous shear modulus (Pa)
G_∞	long-term shear modulus (Pa)
H	Hardness of particle (Pa)
H_i	principal component of Hencky strain in direction i
K_i (where $i = 1, 2, 3, \ldots, n$)	proportionality constants (Equation (12)) (Pa)
L	length of cell extension into micropipette
M_i ($i = 0, 1, 2, 3, \ldots, n$)	proportionality constants (Equation (14)) (Pa)

P	turgor pressure (Pa)
ΔP	micropipette aspiration suction pressure (Pa)
R_c	inner radius of micropipette (m)
R	particle radius (m)
RCF_i	ramp correlation factor
T_1, T_2	tension in the meridian and circumferential directions, respectively (N m^{-1})
V_0	moving speed of the probe (ms^{-1})
X	fractional deformation

GREEK LETTERS

β	C_2/C_1 Mooney–Rivlin material constants
$\gamma^{LW}_{surface}$ $\gamma^{LW}_{foulant}$ γ^{LW}_{fluid}	Lifshitz–van der Waals surface free energies of the surface, foulant and fluid (e.g. water), respectively (N m^{-1})
δ	$\delta = \lambda_2 \sin\psi$ (Equation (26))
ε_i	principal infinitesimal strain component in direction i
ε_∞	strain when the relaxation re-establishes equilibrium (Equation (8))
η	vertical coordinate of cell wall (m)
$\bar{\eta}$	distance between the compression surface and the equatorial plane (m)
η'	derivative of η with respect to ψ
λ_i $(i = 1, 2)$	principal stretch ratio in direction i
λ_0	stretch ratio at the centre of contact area during compression
λ_s	initial stretch ratio
v	Poisson's ratio
ρ	horizontal coordinate of cell wall (m)
$\bar{\rho}$	distance between the η axis and the edge of the cell on the equatorial plane (m)
$\sigma(t)$	time-dependent stress (Pa)
σ_0	stress at time zero (Pa)
σ_∞	stress when the relaxation re-establishes equilibrium (Pa)
σ_i	proportionality constant (Pa)
τ	relaxation time (Equation (8)) (s)
τ_i $(i = 1, 2, \ldots, n)$	relaxation times (Equation (9)) (s)
ψ	the angular position of a point on the cell wall from the vertical axis of symmetry before compression (rad)
ω	derivative of δ with respect to ψ

Γ	the angle of the point on the edge of the contact region between the compression surface and the cell following compression (rad)
Θ	the angle of rotation in the circumferential direction (rad)

ACKNOWLEDGEMENTS

The authors would like to thank Dr T. Liu, Ms M. Liu and Miss J. Xue for allowing using some of their images and data.

REFERENCES

Adams, M. J., and Perchard, V. *Int. Chem. Eng. Symp. Ser.* **92**, 147 (1985).

Ahmad, M. R., Nakajima, M., Kojima, S., Homma, M., and Fukuda, T., IEEE/RSJ International Conference on Intelligent Robots and Systems 1–9, 602 (2007).

Alessandrini, A., and Facci, P. *Meas. Sci. Technol.* **16**, 65 (2005).

Andersson, M., Madgavkar, A., Stjerndahl, M., Wu, Y. R., Tan, W. H., Duran, R., Niehren, S., Mustafa, K., Arvidson, K., and Wennerberg, A. *Rev. Sci. Instrum.* **7**, 78 (2007).

Andrei, D. C., Briscoe, B. J., Luckham, P. F., and Williams, D. R. *J. Chim. Phys. PCB* **93**, 960 (1996).

Arshady, R. *Colloids Surf. A* **153**, 325 (1999).

Aslani, P., and Kennedy, R. A. *J. Microencapsul.* **13**, 601 (1996).

Blewett, J. M., Burrows, K., and Thomas, C. R. *Biotechnol. Lett.* **22**, 1877 (2000).

Born, C., Zhang, Z., Al-Rubeai, M., and Thomas, C. R. *Biotechnol. Bioeng.* **40**, 1004 (1992).

Bos, H. L., and Donald, A. M. *J. Mater. Sci.* **34**, 3029 (1999).

Boudou, T., Ohayon, J., Arntz, Y., Finet, G., Picart, C., and Tracqui, P. *J. Biomech.* **39**, 1677 (2006).

Bowen, W. R., Lovitt, R. W., and Wright, C. J. *J. Colloid Interface Sci.* **237**, 54 (2001).

Boyd, R. D., Verran, J., Jones, M. V., and Bhakoo, M. *Langmuir* **18**, 2343 (2002).

Bryant, Z., Stone, M. D., Gore, J., Smith, S. B., Cozzarelli, N. R., and Bustamante, C. *Nature* **424**, 338 (2003).

Bryers, J. D. *Biotechnol. Prog.* **3**, 57 (1987).

Castelain, M., Pignon, F., Piau, J.-M., and Magnin, A. *J. Chem. Phys.* **128**, 135101 (2008).

Chang, T. M. S. *Ann. N. Y. Acad. Sci.* **875**, 71 (1999).

Chen, M. J., Zhang, Z., and Bott, T. R. *Biotechol. Tech.* **12**, 875 (1998).

Chen, M. J., Zhang, Z., and Bott, T. R. *Colloids Surf. B Biointerfaces* **43**, 59 (2005).

Cheng, L. Y. *J. Biomed. Eng.* **109**, 10 (1987).

Chew, J. Y. M., Cardoso, S. S. S., Paterson, W. R., and Wilson, D. I. *Chem. Eng. Sci.* **59**, 3381 (2004).

Choi, J. B., Inchan, Y., Cao, L., Leddy, H. A., Gilchrist, C. L., Setton, L. A., and Guilak, F. *J. Biomech.* **40**, 2596 (2007).

Christie, A. O., Evans, L. V., and Shaw, M. *Ann. Bot. - Lond.* **34**, 476 (1970).

Cole, K. S. *J. Cell. Comp. Physiol.* **1**, 1 (1932).

Cosgrove, D. J. *Plant. Cell. Environ.* **11**, 67 (1988).

Creely, C. M., Singh, G. P., and Petrov, D. *Opt. Commun.* **245**, 465 (2005).

Daily, B., Elson, E. L., and Zahalak, G. I. *Biophys. J.* **45**, 671 (1984).

DeGroot, A. R., and Neufeld, R. J. *Enzyme Microb. Technol.* **29**, 321 (2001).

Duszyk, M., Schwab, B., Zahalak, G. I., Qian, H., and Elson, E. L. *Biophys. J.* **55**, 683 (1989).

Edwards-Levy, F., and Levy, M. C. *Biomaterials* **20**, 2069 (1999).

Eichhorn, V., Carlson, K., Andersen, K. N., Fatikow, S., and Boggild, P., IEEE/RSJ International Conference on Intelligent Robots and Systems 1–9, 297 (2007).

Fahlbusch, S., Mazerolle, S., Breguet, J. M., Steinecker, A., Agnus, J., Perez, R., and Michler, J. *J. Mater. Process. Technol.* **167**, 371 (2005).

Fairbrother, R. J., and Simmons, S. J. R. *Part. Part. Syst. Char.* **15**, 16 (1998).

Fallman, E., Schedin, S., Andersson, M., Jass, J., and Axner, O., *in* ''Manipulation and Analysis of Biomolecules, Cells and Tissues'' (D. V. Nicolau, J. Enderlein, R. C. Leif, and D. L. Farkas Eds.), Vol. 4962, p. 206, SPIE-INT Society Optical Engineering, Bellingham, USA (2003).

Fan, X., Ten, P., Clarke, C., Bramley, A., and Zhang, Z. *Powder Technol.* **131**, 105 (2003).

Feng, W. W., and Yang, W. H. *Trans. Am. Soc. Mech. Eng.: J. Appl. Mech.* **40**, 209 (1973).

Feng, S. S., Mu, L., Chen, B. H., and Pack, D. *Mat. Sci. Eng. C - Bio. S.* **20**, 85 (2002).

Gaboriaud, F., and Dufrene, Y. F. *Colloids Surf. B* **54**, 10 (2007).

Garrett, T. R., Bhakoo, M., and Zhang, Z. *Biotechnol. Lett.* **30**, 427 (2008).

Gibbs, B. F., Kermasha, S., Alli, I., and Mulligan, C. N. *Int. J. Food. Sci. Nutr.* **50**, 213 (1999).

Goldman, W. H. *Biotechnol. Lett.* **22**, 431 (2000).

Gonzalez-Rodriguez, M. L., Holgado, M. A., Sanchez-Lafuente, C., Rabasco, A. M., and Fini, A. *Int. J. Pharm.* **132**, 225 (2002).

Grigorescu, G., Rosinski, S., Lewinska, D., Ritzén, L. G., Viernstein, H., Teunou, E., Poncelet, D., Zhang, Z., Fan, X., Serp, D., Marison, I., and Hunkeler, D. *J. Microencapsul.* **19**, 641 (2002).

Haddad, Y. M., ''Viscoelasticity of Engineering Materials''. Chapman and Hall, London (1995).

He, J. H., Xu, W., and Zhu, L. *Appl. Phys. Lett.* **90**, 90 (2007).

Hertz, H. *J. Reine Angew. Math.* **92**, 156 (1882).

Hiller, S., Bruce, D. M., and Jeronimidis, G. *J. Texture Stud.* **27**, 559 (1996).

Hiramoto, Y. *Exp. Cell Res.* **32**, 59 (1963).

Hochmuth, R. M. *J. Biomech.* **33**, 15 (2000).

Israelachvili, J. N., ''Intermolecular and Surface Forces''. 2nd ed. Academic Press, London (1992).

Jiang, Q., and Logan, B. E. *Environ. Sci. Technol.* **25**, 2031 (1991).

Jivraj, M., Martini, L. G., and Thomson, C. M. *Pharm. Sci. Technol. Today* **3**, 58 (2000).

Johnson, K. L., ''Contact Mechanics''. Cambridge University Press, Cambridge (1985).

Jones, W. R., Ting-Beall, H. P., Lee, G. M., Kelley, S. S., Hochmuth, R. M., and Guilak, F. *J. Biomech.* **32**, 119 (1999).

Jones, R., Pollock, H. M., Cleaver, J. A. S., and Hodges, C. S. *Langmuir* **18**, 8045 (2002).

Keller, M. W., and Sottos, N. R. *Exp. Mech.* **46**, 725 (2006).

Kikuchi, A., Kawabuchi, M., Sugihara, M., Sakurai, Y., and Okano, T. *J. Control. Release* **47**, 21 (1997).

Kleinig, A. R., Cell Disruption Mechanics, Ph.D. thesis, University of Adelaide, Australia (1997).

Klis, F. M., Boorsma, A., and de Groot, P. W. J. *Yeast* **23**, 185 (2006).

Kotte, M. K., and Rudnic, E. M., Tablet dosage forms, *in* ''Modern Pharmaceutics'' (G. S. Banker Ed.), Informa Healthcare, New York (1995).

Kuen, Y. L., Martin, C. P., and David, J. M. *Adv. Mater.* **13**, 837 (2001).

Kuo, S. C., and Sheetz, M. P. *Science* **260**, 232 (1993).

Kuznetsova, T. G., Starodubtseva, M. N., Yegorenkov, N. I., Chizhik, S. A., and Zhdanov, R. I. *Micron* **38**, 824 (2007).

Lardner, T. J., and Pujara, P., Compression of Spherical Cells, *in* ''Mechanics today'' (S. Nemat-Nasser, Ed.), Vol. 5, p. 161. Pergamon, New York (1980).

Le Meste, M., Champion, D., Roudaut, G., Blond, G., and Simatos, D. *J. Food Sci.* **67**, 2444 (2002).

Lee, K. Y., Peters, M. C., and Mooney, D. J. *Adv. Mater.* **13**, 837 (2001).

Leipzig, Nic. D., and Athanasiou, K. A. *J. Biomech.* **38**, 77 (2005).

Lim, C. T., Zhou, E. H., Li, A., Vedula, S. R. K., and Fu, H. X. *Mater. Sci. Eng.* **26**, 1278 (2006).

Liu, K. K., Williams, D. R., and Briscoe, B. J. *Phys. Rev. E* **54**, 6673 (1996).

Liu, K. K., Wang, H. G., Wan, K. T., Liu, T., and Zhang, Z. *Colloids Surf. B* **25**, 293 (2002a).

Liu, K. K., Chan, V., and Zhang, Z. *Med. Biol. Eng. Comput.* **40**, 491 (2002b).

Liu, W., Christian, G. K., Zhang, Z., and Fryer, P. *Trans. IChemE, Part C* **80**, 286 (2002c).

Liu, T., Donald, A. M., and Zhang, Z. *Mater. Sci. Technol. Ser.* **21**, 289 (2005).

Liu, W., Christian, G. K., Zhang, Z., and Fryer, P. J. *Int. Dairy J.* **16**, 164 (2006a).

Liu, W., Fryer, P. J., Zhang, Z., Zhao, Q., and Liu, Y. *Innovative Food Sci. Eng. Technol.* **7**, 263 (2006b).

Liu, W., Aziz, N. Ab., Zhang, Z., and Fryer, P. J. *J. Food Eng.* **78**, 217 (2007).

Logan, B. E., and Kilps, J. R. *Water Res.* **29**, 443 (1995).

Lu, G. Z., Thompson, F. G., and Gray, M. R. *Biotechnol. Bioeng.* **40**, 1277 (1992).

Lulevich, V. V., Radtchenko, I. L., Sukhorukov, G. B., and Vinogradova, O. I. *J. Phys. Chem. B* **107**, 2735 (2003).

Lulevich, V., Zink, T., Chen, H. Y., Liu, F. T., and Liu, G. Y. *Langmuir* **22**, 8151 (2006).

Madene, A., Jacquot, M., Scher, J., and Desobry, S. *Int. J. Food. Sci. Technol.* **41**, 1 (2006).

Madgar, l., Seidman, D. S., Levran, D., Yonish, M., Augarten, A., Yemini, Z., Mashiach, S., and Dor, J. *Hum. Reprod.* **11**, 2151 (1996).

Marszalek, P. E., Oberhauser, A. F., Pang, Y. P., and Fernandez, J. M. *Nature* **396**, 661 (1998).

Martinsen, A., Skjakbraek, G., and Smidsrod, O. *Biotechnol. Bioeng.* **33**, 79 (1989).

Mashmoushy, H., Zhang, Z., and Thomas, C. R. *Biotechnol. Tech.* **12**, 925 (1998).

Masuda, T., Ingram, A., Zhang, Z., and Seville, J. P. K., 13th World Clean Air and Environmental Protection Congress and Exhibition, London, UK, paper number 461 (2004).

Mattice, J. M., Lau, A. G., Oyen, M. L., and Kent, R. W. *J. Mater. Res.* **21**, 2003 (2006).

Mendelson, N. H., Sarlls, J. E., Wolgemuth, C. W., and Goldstein, R. E. *Phys. Rev. Lett.* **84**, 1627 (2000).

Michaels, J. D., Petersen, J. F., McIntire, L. V., and Papoutsakis, E. T. *Biotechnol. Bioeng.* **38**, 169 (1991).

Middelberg, A. P. J. *Biotechnol. Adv.* **13**, 491 (1995).

Mills, J. P., Qie, L., Dao, M., Lim, C. T., and Suresh, S. *Mol. Cell Biol.* **1**, 169 (2004).

Mow, V. C., Kuei, S. C., Lai, W. M., and Amstrong, C. G. *ASME J. Biomech. Eng.* **102**, 73 (1980).

Müller, E., Chung, J. T., Zhang, Z., and Sprauer, A. *J. Chromatogr. A* **1097**, 116 (2005).

Murhammer, D. W., and Goochee, C. F. *Biotechnol. Prog.* **6**, 391 (1990).

Nakabayashi, D., and Silva, P. C. *Int. J. Nanotechnol.* **4**, 609 (2007).

Nguyen, V. B., Wang, C. X., Thomas, C. R., and Zhang, Z. *Chem. Eng. Sci.* **64**, 821 (2009).

Nishizaka, T., Miyata, H., Yoshikawa, H., Ishiwata, S., and Kinosita, K. *Nature* **377**, 251 (1995).

Ohtsubo, T., Tsuda, S., and Tsuji, K. *Polymer* **32**, 2395 (1991).

Papoutsakis, E. T. *Trends Biotechnol.* **9**, 427 (1991).

Pelling, A. E., Sehati, S., Gralla, E. B., Valentine, J. S., and Gimzewski, J. K. *Science* **305**, 1147 (2004).

Poncelet, D., and Neufeld, R. T. *Biotechnol. Bioeng.* **33**, 95 (1989).

Read, T., Stensvaag, V., Vindenes, H., Ulvestad, E., Bjerkvig, R., and Thorsen, F. *Int. J. Neurosci.* **7**, 653 (1999).

Rehor, A., Canaple, L., Zhang, Z., and Hunkeler, D. *J. Biomater. Sci. Polym.* **12**, 157 (2001).

Ren, Y., Donald, A. M., and Zhang, Z. *Mater. Sci. Technol. Ser.* **23**, 857 (2007).

Ren, Y. L., Donald, A. M., and Zhang, Z., *Scanning* **30**, 435 (2008).

Ribeiro, A. J., Neufeld, R. J., Arnaud, R. J., and Chaumeil, J. C. *Int. J. Pharm.* **187**, 115 (1999).

Roberts, R. J., and Rowe, R. C. *Chem. Eng. Sci.* **42**, 903 (1987).

Rubinstein, M. H., "Pharmaceutics, The Science of Dosage Form Design". Churchill Livingstone, Edinburgh (2000).

Schuldt, U., and Hunkeler, D. *Minerva Biotecnol.* **12**, 249 (2000).

Shamlou, P. A., and Titchener-Hooker, N., Turbulent aggregation and breakup of particles in liquids in liquids in stirred vessels, *in* "Processing of Solid–Liquid Suspensions" (P. A. Shamlou Ed.), pp. 1–25. Butterworth-Heinemann Ltd, Oxford (1993).

Sharp, J. M., Duran, R. S., and Dickinson, R. B. *J. Colloid Interface Sci.* **299**, 180 (2006).

Shieh, A. C., and Athanasiou, K. A. *J. Biomech.* **39**, 1595 (2006).

Shiu, C., Zhang, Z., and Thomas, C. R. *Biotechnol. Tech.* **13**, 707 (1999).

Sindel, U., and Zimmermann, I. *Powder Technol.* **117**, 247 (2001).

Smith, S. B., Cui, Y., and Bustamante, C. *Science* **271**, 795 (1996).

Smith, A. E., Moxham, K. E., and Middelberg, A. P. J. *Chem. Eng. Sci.* **53**, 3913 (1998).

Smith, A. E., Zhang, Z., and Thomas, C. R. *Chem. Eng. Sci.* **55**, 2031 (2000a).

Smith, A. E., Moxham, K. E., and Middelberg, A. P. J. *Chem. Eng. Sci.* **55**, 2043 (2000b).

Sorensen, B. F., Horsewell, A., Jorgensen, O., and Kumar, A. N. *J. Am. Ceram. Soc.* **81**, 661 (2001).

Stenekes, R. J. H., De Smedt, S. C., Demeester, J., Sun, G. Z., Zhang, Z. B., and Hennink, W. E. *Biomacromolecules* **1**, 696 (2000).

Stocks, S. M., and Thomas, C. R. *Biotechnol. Bioeng.* **75**, 702 (2001).

Stokes, D. J., and Donald, A. M. *J. Mater. Sci.* **35**, 599 (2000).

Strand, B. L., Morch, Y. A., and Skjak-braek, G. S. *Minerva Biotecnol.* **12**, 223 (2000).

Sugimoto, T., Takahashi, T., Itoh, H., Sato, S., and Muramatsu, A. *Langmuir* **13**, 5528 (1997).

Sun, G., and Zhang, Z. *J. Microencapsul.* **18**, 593 (2001).

Sun, G., and Zhang, Z. *Int. J. Pharm.* **242**, 307 (2002).

Tang, S., Preece, J. M., McFarlane, C. M., and Zhang, Z. *J Colloid Interface Sci.* **221**, 114 (2000).

Tatara, Y. *J. Eng. Mater. - Trans. ASME* **113**, 285 (1991).

Tatara, Y. *J. Eng. Mater. - Trans. ASME* **36**, 190 (1993).

Thiel, B. L., and Donald, A. M. *Ann. Bot. - Lond.* **82**, 727 (1998).

Thomas, C. R., Al-Rubeai, M., and Zhang, Z. *Cytotechnology* **15**, 329 (1994).

Thomas, C. R., Zhang, Z., and Cowen, C. *Biotechnol. Lett.* **22**, 531 (2000).

Tomos, D. *Biotechnol. Lett.* **22**, 437 (2000).

Tomos, A. D., and Leigh, R. A. *Annu. Rev. Plant Phys.* **50**, 447 (1999).

Torre, M. L., Maggi, L., Vigo, D., Galli, A., Bornaghi, V., Maffeo, G., and Conte, U. *Biomaterials* **21**, 1493 (2000).

Touhami, A., Nysten, B., and Dufrene, Y. F. *Langmuir* **19**, 4539 (2003).

Van Raamsdonk, J. M., and Chang, P. L. *J. Biomed. Mater. Res.* **54**, 264 (2001).

Vandenberg, G. W., Drolet, C., Scott, S. L., and Noue, J. de la. *J. Control. Release* **77**, 297 (2001).

Wang, C. X., Wang, L., and Thomas, C. R. *Ann. Bot. - Lond.* **93**, 443 (2004).

Wang, C. X., Cowen, C., Zhang, Z., and Thomas, C. R. *Chem. Eng. Sci.* **60**, 6649 (2005).

Wang, C. X., Pritchard, C. R., and Thomas, C. R. *J. Texture Stud.* **37**, 597 (2006a).

Wang, L., Hukin, D., Pritchard, J., and Thomas, C. R. *Biotechnol. Lett.* **28**, 1147 (2006b).

Ward, I. M., and Hadley, D. W., "An Introduction to the Mechanical Properties of Solid Polymers". Wiley, Chichester, UK (1993).

Watkinson, A. P., Müller-Steinhagen, H., and Malayeri, M. R., Heat Exchanger Fouling and Cleaning: Fundamentals and Applications, ECI Symposium Series, Vol. RP1, Bypress Publications, Berkeley, USA (2004).

Weiss, L. *Exp. Cell Res.* **8**, 141 (1961).

Welsh, J. P., Relationships between Hybridoma Cell Mechanical Properties and Physiology, Ph.D. thesis, The University of Birmingham (1998).

Willett, C. D., Zhang, Z., and Seville, J. P. K., "The 1997 IChemE Research Event", Vol. 1, p. 401. Chameleon Press Ltd., London (1997).

Wilson, D. I., Fryer, P. J., and Hasting, A. P. M., ''Fouling, Cleaning and Disinfection in Food Processing''. University of Cambridge, Cambridge, UK, p. 263 (2002).

Wu, H., Spence, R. D., Sharpe, P. J. H., and Goeschl, J. D. *Plant Cell Environ.* **8**, 563 (1985).

Xie, C., and Li, Y. *J. Appl. Phys.* **93**, 2982 (2003).

Xue, J., Novel Encapsulation of Active Ingredients for Dental Care, Ph.D. thesis, University of Birmingham, UK (2008).

Xue, J., and Zhang, Z. *J. Microencapsul.* **25**, 523 (2008).

Yap, S. F., Adams, M., Seville, J., and Zhang, Z. *China Particuology* **4**, 35 (2006).

Yap, S. F., Adams, M. J., Seville, J. P. K., and Zhang, Z. *Powder Technol.* **185**, 1 (2008).

Yeung, A. K. C., and Pelton, R. J. *Colloid Interface Sci.* **184**, 579 (1996).

Yoneda, M. *J. Exp. Biol.* **41**, 893 (1964).

Yoneda, M. *Adv. Biopys.* **4**, 153 (1973).

Yu, M. F., Dyer, M. J., Skidmore, G. D., Rohrs, H. W., Lu, X. K., Ausman, K. D., Von Her, J. R., and Ruoff, R. S. *Nanotechnology* **10**, 244 (1999).

Zhang, J., and Buffle, J. *Colloids Surf. A* **107**, 175 (1996).

Zhang, Z., Ferenczi, M. A., and Thomas, C. R. *Chem. Eng. Sci.* **47**, 1347 (1992a).

Zhang, Z., Al-Rubeai, M., and Thomas, C. R. *Enzyme Microb. Technol.* **14**, 980 (1992b).

Zhang, Z., Saunders, R., and Thomas, C. R. *J. Microencapsul.* **16**, 117 (1999).

Zhao, L., and Zhang, Z. *Artif. Cell Blood Sub.* **32**, 25 (2004).

Zhao, Q., Wang, S., and Müller-Steinhagen, H. *Appl. Surf. Sci.* **230**, 371 (2004).

Zhao, L., Schaefer, D., Xu, H. J., Modi, S. J., Lacourse, W. R., and Marten, M. R. *Biotechnol. Prog.* **21**, 292 (2005).